ACS APPLIED ELECTRONIC MATERIALS

pubs.acs.org/acsaelm

Spotlight on Applications

Comprehensive Model of Electron Conduction in Oxide-Based Memristive Devices

Carsten Funck and Stephan Menzel*

Cite This: *ACS Appl. Electron. Mater.* 2021, 3, 3674−3692

Read Online

ACCESS | Metrics & More | Article Recommendations

ABSTRACT: Memristive devices are two-terminal devices that can change their resistance state upon application of appropriate voltage stimuli. The resistance can be tuned over a wide resistance range enabling applications such as multibit data storage or analog computing-in-memory concepts. One of the most promising classes of memristive devices is based on the valence change mechanism in oxide-based devices. In these devices, a configurational change of oxygen defects, i.e. oxygen vacancies, leads to the change of the device resistance. A microscopic understanding of the conduction is necessary in order to design memristive devices with specific resistance properties. In this paper, we discuss the conduction mechanism proposed in the literature and propose a comprehensive, microscopic model of the conduction mechanism in this class of devices. To develop this microscopic picture of the conduction, ab initio simulation models are developed. These simulations suggest two different types of conduction, which are both limited by a tunneling through the Schottky barrier at the metal electrode contact. The difference between the two conduction mechanisms is the following: for the first type, the electrons tunnel into the conduction band and, in the second type, into the vacancy defect states. These two types of conduction differ in their current voltage relation, which has been detected experimentally. The origin of the resistive switching is identical for the two types of conduction and is based on a modification of the tunneling distance due to the oxygen vacancy induced screening of the Schottky barrier. This understanding may help to design optimized devices in terms of the dynamic resistance range for specific applications.

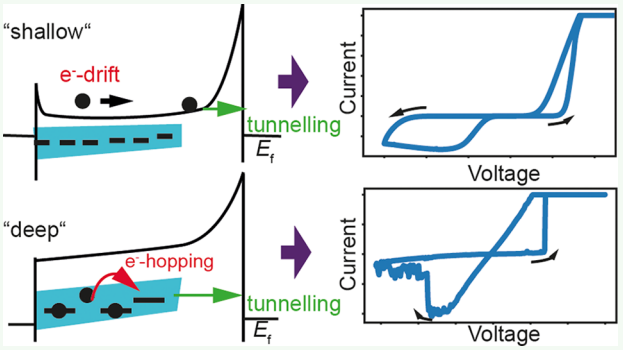

KEYWORDS: *memristor, ReRAM, electron conduction, valence change memory, redox-based memories*

INTRODUCTION

Memristive devices, in general, describe an electronic device that can switch between different resistive states upon appropriate voltage stimuli. The programmed resistance states are typically nonvolatile. Due to this property, memristive devices have been investigated for nonvolatile binary and multibit memories.[1−5] Recently, memristive devices have been exploited for computing-in-memory (CIM) applications.[6−12] It was, for example, shown that a vector matrix multiplication can be performed in one step in a memristive memory array by exploiting Kirchhoff's laws.[13,14] This operation principle can be used for a mixed-precision computing paradigm,[15] image compression,[16] and for machine learning approaches using backpropagation or spiking neural networks.[17−20] Moreover, Boolean logic gates and further arithmetic operations can be realized.[21−48] The memristive switching phenomenon can be realized by different physical means, giving rise to different types of memristive devices. In phase change memories, the device is switched between an amorphous and crystalline phase showing different resistance by Joule heating.[49] In spin-transfer-torque-magnetic-RAMs (STT-MRAMs), a tunneling barrier is modulated by the parallel/antiparallel magnetization of two ferromagnetic layers, of which one layer can switch its magnetization by spin-polarized currents.[50] In ferroelectric tunnel junctions, the height of a tunneling barrier is modulated by the orientation of the adjacent ferroelectric material, whose remanent polarization can be switched by bipolar voltage pulses.[51] Another class of memristive devices are the redox-based memristive switching devices, which rely on the motion of ionic defects and concurrent redox reactions.[1] Electrochemical metallization cells (also called conductive bridging random access memories), for example, rely on the electrochemical formation or dissolution of a (typically) Ag or Cu filament within a host insulating layer. In valence change memory (VCM) cells, the memristive switching is induced by

Received: April 30, 2021
Accepted: July 19, 2021
Published: September 7, 2021

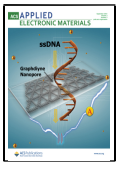

https://doi.org/10.1021/acsaelm.1c00398
ACS Appl. Electron. Mater. 2021, 3, 3674−3692

the motion of oxygen defects and concurrent redox reactions in an oxide layer. All of these devices show the memristive switching phenomenon but with a different dynamic range of resistance. The dynamic resistance range can be tuned by the operating conditions but are also strongly linked to the switching mechanism and the properties of the used materials. STT-MRAMs, for example, show only two (very) stable resistance states with a very small resistance ratio (less than 1 order of magnitude). In contrast, the resistance of VCM cells can be tuned over a large resistance range but show a distribution of the resistance states. For the CIM applications mentioned before, the requirements of the dynamic resistance range differ. Thus, for a certain CIM application one device type might be most appropriate whereas another type is better suited for another application. For implementing memristive Boolean logic gates and functions of higher complexity such as adders or multipliers, binary memristive switching devices are considered.[42,44,52] In this case, the two states need to be clearly distinguishable. Thus, a high resistance ratio may be beneficial, especially if the memristive array is operated without a transistor, but with a nonlinear selector device at each node. Binary memristive devices have been also proposed for binarized neural networks or in compound synapses.[53,54] In this case, some resistance overlap may not deteriorate the function but is even beneficial in order to mimic an analog behavior. If single memristive devices are exploited as single analog synapses in artificial neural networks, the devices should show easily programmable analog resistance states. In addition, a wide modulation range is desired. In any case, it is important to understand the underlying conduction mechanism to design it with respect to the target application.

In this spotlight, we discuss the physical nature of the conduction mechanism in VCM type of devices. These devices are investigated a lot for CIM applications as they offer a large dynamic resistance range, ease of fabrication, CMOS compatibility, and low energy consumption. While it is generally accepted that the change of the oxygen defect configuration leads to a resistance change, different physical models of the conduction mechanism have been proposed. Here, after a brief introduction to VCM devices, we review the proposed conduction models and discuss them critically. Then, we propose a consistent picture of the conduction mechanisms which is related to the nature of the defect state induced by oxygen vacancies in a specific oxide material.

MEMRISTIVE SWITCHING IN VCM CELLS

VCM devices typically consist of a metal/oxide/metal stack. The oxide layer is build out of a binary (e.g., HfO_2, Ta_2O_5, WO_3, or TiO_2) or ternary transition metal oxide (e.g., $SrTiO_3$, $SrZrO_3$, or $BiFeO_3$). Also bilayer stacks of different oxide materials have been used. To achieve a stable bipolar switching mode two different metals are used as electrodes. One electrode consists of an inert metal, such as Pt, Ir, or TiN. This metal forms a high electrostatic barrier with the oxide material. The second electrode consists of an oxidizable metal such as W, Ta, Ti, or Hf.[55] This electrode typically forms an ohmic contact with the oxide material. For the most commonly used oxide materials, the conductivity increases for an increasing oxygen deficiency. For a crystalline oxide material, this change in conductivity can be explained by point defect chemistry.[56,57] The missing oxygen ions in the oxide matrix are described as oxygen vacancies, which are doubly positively charged with respect to the lattice. This excess positive charge can be compensated by two electrons. These electrons are typically localized in the d-orbitals of the cation sublattice, leading to a change of the valence state of the transition metal cations. This mechanism gives the name of this class of memory: the valence change memory (VCM). As fabricated, the oxides are typically stoichiometric. An initial so-called electroforming step is required to extract oxygen from the oxide layer, i.e. introducing oxygen vacancies. This is accomplished by an oxygen exchange reaction at one of the two metal/oxide interfaces.[1,58−60] For binary oxides, typically a positive voltage is applied to the oxidizable electrode. After the electroforming step, the device can be switched between different resistance states by applying appropriate voltage stimuli. It is generally accepted that the switching effect relies on the redistribution of the oxygen vacancies under an applied electric field.[1,61−66] It should be noted that due to the different work functions of the metals, the change of the total resistance depends also on the location of the oxygen vacancies. As the oxygen vacancy acts as mobile donor and is positively charged, it influences also the shape of the electrostatic barriers at the metal/oxide interface. Thus, an oxygen vacancy close to the electrode with the higher work function will lead to a stronger resistance change than close to the oxidizable electrode. Therefore, the metal electrode with the higher work function is also called electronically active electrode (short: active electrode) as the resistance switching is assumed to take place due to changes of the oxygen vacancy concentration close to this interface. As the ions are charged, the switching mechanism is inherently bipolar. The switching polarity, however, is related to the dominated means of the defect redistribution. If the ions are mainly redistributed via ionic motion within the oxide material, the switching from the high resistance state (HRS) to the low resistance state (LRS)—called SET transition—is accomplished by applying a negative voltage to the active electrode. If the switching relies dominantly on an oxygen exchange at the active electrode, the SET transition is caused by applying a positive voltage to the active electrode.[67] While the forming switching polarity is called counter-eightwise switching (named after the sense of the polarity of the $I-V$ curve), the latter is called eightwise switching. It has been demonstrated that both switching modes can appear in the same device just by changing the operating conditions.[68] For the present work, we only consider the static configuration and not the dynamics, in order to discuss the conduction mechanism independently from a vacancy redistribution. One needs to consider, however, that the description of the different conduction states needs to be consistent with the idea of the reconfiguration of the oxygen defects. It should be noted that in state-of-the-art VCM cells, which show reproducible switching with high speed at comparably low voltages, the oxide layer is very thin and asymmetric electrode materials are used.[69−72]

Comparing different $I-V$ characteristics of VCM devices in the literature, one can distinguish at least two types of curves as shown in Figure 1. Figure 1a shows a resistive switching curve of a Nb:$SrTiO_3$/$SrTiO_3$/Pt device cell of micrometer sized electrodes. Figure 1b the resistive switching of a Ti/HfO_2/Pt cell with a nanometer sized electrode. The fabrication and measurement details are described more precisely in the Methods section. While the type 1 curve (Figure 1a) shows very nonlinear (exponential), asymmetric $I-V$ characteristics with respect to the voltage polarity, the type 2 curve is rather symmetric and much more linear. Examples for such a strong

https://doi.org/10.1021/acsaelm.1c00398
ACS Appl. Electron. Mater. 2021, 3, 3674−3692

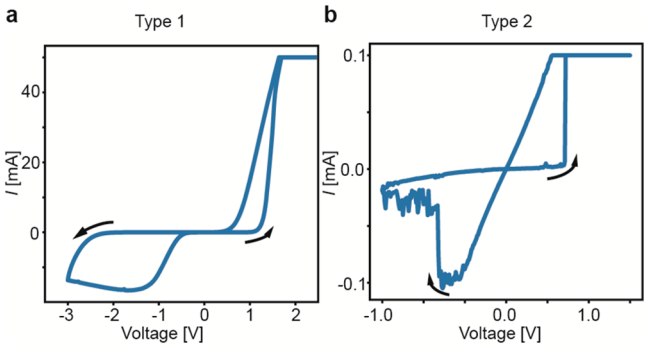

Figure 1. (a) Type 1 conduction in a Nb:$SrTiO_3$/$SrTiO_3$/Pt resistive switching cell (cf. Methods section and data taken from ref 100) on the left. The signal is applied to the Pt electrode (eightwise (8w) switching polarity). (b) Type 2 conduction in a Ti/HfO_2/Pt resistive switching cell on the right. The signal is applied to the Ti electrode; cf. the Methods section for details (couter-eightwise (c8w) switching polarity).

nonlinear conduction of type 1 are reported frequently in the literature.[68,73−78] In the second type of conduction, the nonlinearity in the same voltage range (≈0.1−1 V) is clearly weaker and example $I-V$ curves are reported as well.[74,79−89]

The type of curve is related to the used materials. The strong exponential type 1 is often found in Ti-based perovskite oxide materials, such as $SrTiO_3$, $BaTiO_3$, $CaTiO_3$, or $Mg_{0.5}Ca_{0.5}TiO_3$.[90−93] In addition, also perovskites without Ti cations, like $BiFeO_3$, tend to show a type 1 $I-V$ curve.[73,75] For the resistive switching in TiO_2 the same behavior is detected while not having a perovskite structure.[68] In addition, the conduction in resistive switching VCM cells based on In_2O_3 and SnO_2 show the type 1 conduction.[94,95] The widely used material HfO_2 has been identified as type 2 conduction material, but also other materials such as Ta_2O_5, Nb_2O_5, ZrO_2, or Lu_2O_3[79,82,83,96,97] show this type of conduction. This material dependence suggest that there is a difference on the microscopic level, which determines the type of the $I-V$ curve.

In this spotlight the focus is on VCM cells, with the bipolar characteristics. However, the TCM unipolar switching is strongly connected.[1] Consequently, it might be possible that greater parts of the analysis in this article could be also applied for unipolar devices. For example, the HRS characteristics of a unipolar switching $Ba_{0.7}Sr_{0.3}TiO_3$[98] show type 1 conduction like behavior. Moreover, the second type of conduction properties was found in HfO_2 based unipolar switching cells.[99]

■ ANALYSIS OF THE CONDUCTION MECHANISM

To identify the conduction mechanism of the VCM device under test, the investigation of one switching curve is not conclusive. In fact, a combination of different experiments is required. The voltage dependence for both voltage polarities needs to be investigated. Moreover, the temperature dependence should be investigated as well. This should be performed for the LRS and the HRS but, ideally, for all possible intermediate resistance states. A major challenge of this analysis is that the state of the device is static, i.e. the oxygen defect configuration should be frozen in for the time of the experiment. This limits the experiment to small voltages and limits the temperature range that can be evaluated. For the analysis of the conduction mechanism, one can try to fit different conduction models to the experimental data sets. One attempt is to fit the slopes in $\log(I)-\log(V)$ to different models. This method can only be considered as first indication. For a conclusive result one should extract all fitting parameters and check if they are physically reasonable. For example in a worst case, the slope fits but this could only be achieved if the assumed distance between traps are smaller than interatomic distances. Another challenge is that the conduction may be controlled by a combination of conduction mechanisms. In filamentary VCM cells, the surrounding matrix may contribute to the total resistance in the HRS state. In addition, it is conceivable that at low voltage the metal/oxide interface limits the conduction, but at higher voltages the filament resistance itself determines the overall resistance. Finally, when the conduction mechanism of the different states should be consistent, the transition from one mechanism to another one should occur by changing the defect configuration only. In the following, we review the different conduction mechanisms that have been discussed in the literature, i.e. trap-assisted tunneling, space-charge limited current, Poole−Frenkel conduction, and Schottky-barrier related conduction mechanisms.

A. Trap-Assisted Tunneling. A promising candidate to explain the conduction in VCM cells is an electron trap based tunneling transport. It is accepted, in general, that the oxygen vacancies form a donorlike defect state, and these defect states result from the cationic states of the oxide. Due to the high band gap, the energetic distance to the conduction band could be significant. For instance, in HfO_2, the defect state is reported to be located more than 2 eV below the conduction band for neutral and single charged oxygen vacancies.[101−104] As a result, the donor activation energy is comparably high and it is likely that electrons could be trapped in the defect state. Nevertheless for a finite current, electrons must be transferred from one to the other electrode. To contribute to the current, the trapped electrons must be released. One opportunity is that these electrons are thermally excited into the conduction band, which is the basis of the later discussed Poole-Frenkel effect. The other method is that the electrons tunnel from one trap state to other free trap states (i.e., the oxygen vacancy induced defect states).

Finally, a trap state is reached from which the electrons tunnel into the next electrode. This transport is called trap-assisted tunneling (TAT) and is sketched in Figure 2.

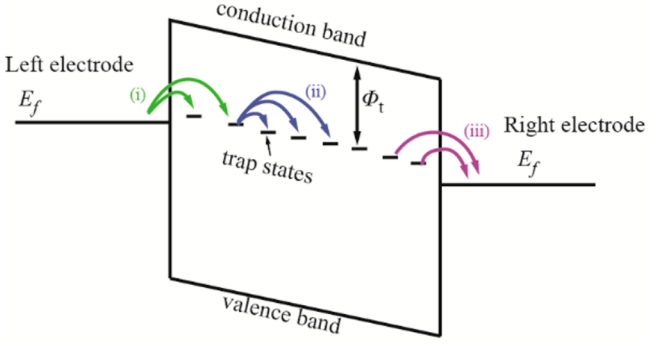

Figure 2. Schematic sketch of trap assisted tunneling transport. Here the Fermi levels in the left and right electrode are separated by the applied voltage. The induced field generates a tilted rectangular band structure. The traps are found in the band gap by ϕ_t below the conduction band. To transport an electron three steps are required: (i) tunneling into the trap from one electrode, (ii) tunneling from trap-to-trap, and (iii) tunneling from the trap into the other electrode.

https://doi.org/10.1021/acsaelm.1c00398
ACS Appl. Electron. Mater. 2021, 3, 3674−3692

This type of transport can be divided into three processes: (i) the tunneling from the electrode into the trap, (ii) the tunneling from trap to trap, and (1) the tunneling from the trap into the electrode. In all three cases, the tunneling levels could differ. Therefore, a tunneling into an energetic higher level requires a thermal excitation. The representative energy level for the electrodes is the quasi Fermi level in the metals. TAT has been identified as the dominating leakage current in insulating thin oxide films.[105−108] Furthermore, many studies reported TAT transport or used it as a conduction mechanism in simulation studies.[109−115,115−124] Even these studies could be summarized under the umbrella of TAT, but the details in the suggested transport mechanism differ significantly. The review of all of them would exceed the extent of this article, but a few of them are explained in the following, including the TAT based space charge limited current in the SCLC subsection.

A popular method to describe TAT is given by Houng et al.,[125] who derived the relation

$$j \propto \exp\left[-\frac{4\sqrt{2qm_{ox}}}{3\hbar}\phi_t^{3/2}\frac{1}{F}\right] \quad (1)$$

with the charge q, the effective mass m_{ox} of the electrons in the oxide, the Planck constant $\hbar$, the trap level ϕ_t, and the electric field F. In this theory, the transport of electrons from one electrode to the other electrode is supposed to go over one trap only. The tunneling from trap to trap, however, is neglected. Also, the thickness of the oxide layer and the trap distance are not considered, which makes the model oversimplified. Despite these issues, this equation is frequently used to explain the conduction in resistive switching VCM cells. By fitting eq 1 to the experimental data, the trap state energy can be calculated.[113,126−128]

This analysis has been applied in a highly interesting study by Beilliard et al. to fit the HRS and the LRS conduction of a TiN/Al_2O_3 (1.4 nm)/TiO_{2-x} (30 nm)/Pt device for very small temperatures as shown in Figure 3.[113] The low temperatures allowed them to decouple the trap-assisted tunneling from thermally activated conduction mechanisms. Thereby, two different trap levels were extracted for each of the two resistance states. In fact, this is the only way to explain the different states as other quantities such as trap distance or oxide thickness are not considered. The authors suggested that the change in the trap states induces the resistive switching. The origin of the change of the trap states (levels) is related to a change in the oxygen vacancy concentration. It is assumed that the oxygen vacancy concentration reduces locally (as usual) close to one electrode interface. According to eq 1, however, the transport is given by a constant electric field. Having a resistance dominating local gap of reduced oxygen vacancy content would lead to a voltage drop over this small region. As a result, the homogeneous field used for eq 1 is not consistent to a local gap of oxygen vacancies. This means that the model does not allow quantification of the defect concentration.

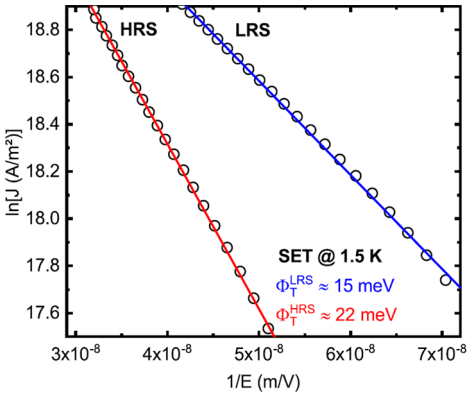

Figure 3. Fit of eq 1 to the HRS and LRS of a TiN/Al_2O_3(1.4 nm)/TiO_{2-x} (30 nm)/Pt. The solid lines are the insets, and the black circles are the data points (Adapted from the work of Beilliard et al.[113] https://creativecommons.org/licenses/by/4.0/).

In general, VCM cells are bipolar switching devices with a distinct switching polarity. This requires an asymmetry in the conduction with respect to the defect configuration. This means that either the defect configuration is strongly asymmetric and/or the change of the defect concentration at the two metal/oxides causes differently strong current responses. Furthermore, the $I-V$ curve is polarity dependent, too. This asymmetry does not favor a bulk transport mechanism, as this considers a homogeneous, polarity-independent field or voltage drop. In fact, symmetric VCM cells with identical or similar electrodes show a very special switching behavior, which is known as complementary switching,[129−132] rather than a clearly defined bipolar operation. Furthermore, the electrodes do have a significant influence on the electronic transport as discussed in the introduction to VCM cells. Moreover, electrodes with different work functions generate an internal built-in potential, which should be considered for the discussion of the electron conduction mechanism. The issues mentioned above are related in general to all bulk transport mechanisms, such as the space charge limited current TAT mechanism (see next section), near range hopping, or variable range hopping.

Yu et al.[115,118,120] proposed an interface limited TAT transport mechanism that solves the issues mentioned before. Here, the total current is limited by tunneling from/into one of the electrodes and not by the trap-to-trap hopping within the bulk. In the sense of Figure 2, the transport is limited by mechanism i or iii. Consequently, this transport is asymmetric as expected based on the observed bipolar switching characteristic. Note that this is only true when the current is limited at one electrode and not identical at both electrodes. In these cases a symmetric complementary switching is expected.

Another study of Matveyev et al.[133] is highly interesting for this conduction mechanism review. Using a $TiN/HfO_2/TiN$ VCM cell, they explained the measured data successfully using the model of Yu et al. The TAT transport mechanism was also proven in a sophisticated experiment by Yalon et al.[134] The resistive switching cell is used as the basis in an InGaAs based bipolar transistor. In this setup, the band structure of the InGaAs allows identification of the energy level for the current transport which reveals that the conduction level is fit to a trap-assisted transport mechanism, consistent with the interface-limited trap assisted tunneling.

B. Space-Charge Limited Current. The $I-V$ dependence in a couple of VCM systems can be interpreted as nonexponential (type 2) in the voltage range of switching, but the $I-V$ dependence is also not linear (no ohmic behavior). As a consequence, the conduction cannot be described by a mechanism based on a thermal excitation process with a voltage modulated thermal barrier. The popular

https://doi.org/10.1021/acsaelm.1c00398
ACS Appl. Electron. Mater. 2021, 3, 3674−3692

Boltzmann approximation of the Fermi−Dirac distribution for the thermal excitation of electrons in those mechanisms results in exponential $I-V$ characteristics with strong temperature dependence. On the other hand, a simple band transport leads to linear $I-V$ characteristics. Hence, an alternative conduction mechanism with nonexponential voltage dependence is required. Such a characteristic is found in the space-charge limited current (SCLC) model, which is frequently used to explain the transport in VCM cells.[97,97,135−150]

The principle of space-charge limited current is given by the charge transport (here electrons) between two electrodes with a potential difference. The electric field between the electrodes leads to an acceleration of the electrons. Note that the acceleration is only true in a vacuum, for which this transport mechanism was originally derived.[151,152] Later this mechanism was adapted to solids.[153] The applied electric field induces an electron flow and thereby the electronic current. The current is determined by the electron velocity. The finite velocity of the electrons has the effect that the electrons are located in the space between the two electrodes, until they reach the anode. This residence time of the electrons in the space between the two electrodes equilibrates to a space charge distribution. The electric field generated by the space charge counteracts the applied electric field. As a consequence, the space charge starts to limit the total current flow. For a simple model of two planar electrodes in a vacuum this leads to a power law of $I \propto V^{3/2}$.[151,152] In the case of a VCM cell, there is an oxide between the two electrodes. Thus, the transport velocity is also determined by the electron mobility μ in these materials. In this case, the power law becomes parabolic and the current is also proportional to the electron mobility $I \propto \mu V^2$.[154,155]

To verify this type of conduction, the $I-V$ dependence is measured and plotted on a double logarithmic scale, which allows determination of the power law $I \propto V^{\alpha}$ by a linear regression.[97,97,135−150] An example from the work of Maikap[141] of this approach is shown in Figure 4 for a W/TaO_x/TiN cell. The slopes α determined in resistive switching devices differ strongly, and the values in the referenced literature are found between 0.8 and 21.[135,136]

Often, more than one slope is fitted to the $I-V$ measurements at different voltage ranges, cf. Figure 4. In the majority of the studies the parabolic dependence of $\alpha = 2$ is not found. The parabolic dependence, however, assumes a trap free solid with a band transport mechanism. In presence of deep electron traps, the space charge distribution changes. In this case, the power law changes to $I \propto V^{\alpha}$ with an α value, which depends on the trap density.[155,156] Hence, it is a condition for the SCLC without parabolic behavior ($\alpha \neq 2$) that the SCLC originates from trap-to-trap transport.

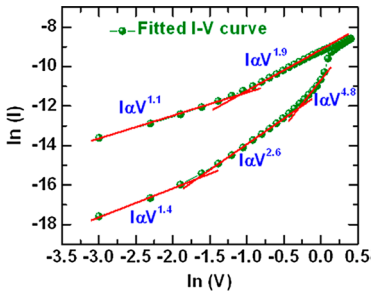

Figure 4. Double logarithmic plot of the $I-V$ curve at an SET event for a W/TaO_x/TiN cell, with an oxide thickness of 7 nm, cf. ref 141. The green dots are the measured current responses, and the red curve is the linear regression fit to the data. The linear regression has been applied to several voltage ranges (Reprinted from the work of Maikap et al.[141] https://creativecommons.org/licenses/by/4.0/).

From this point of view it is a subclass of the general TAT transport and thus a promising approach to explain the current transport. There are, however, some issues related to the SCLC model. The oxygen vacancy concentration during the switching changes and is therefore unknown and probably not homogeneously distributed, which is an assumption in the derivation of the power law $I \propto V^{\alpha}$. In many VCM cells, the active oxide layer is in the range of a couple of nanometers and it is unlikely that the concentration could be treated as constant over a sufficiently long distance. Moreover, the derivation of the SCLC model assumes that two ohmic interfaces are formed. This is reasonable for very thick films, but for oxides of a few nanometers as in the state-of-the-art VCM cells this assumption does not seem to be reasonable. The asymmetry of the electrodes, i.e. the different work functions, is neglected as well. Moreover, the space charge in the SCLC model is only formed by the free electrons. The net background charge due to oxygen vacancy defects is neglected. This assumption holds only valid if the amount of electrons in the system is much higher than the amount of oxygen vacancies. As the amount of oxygen vacancies is quite high in VCM cells, this assumption appears to be invalid for state-of-the-art VCM cells. It might be fulfilled, however, for very thick devices with large electrode areas and low defect concentration. For SCLC, the layer thickness must at least exceed the screening distance of the electrodes by a few times.

Another problem is the fitting in different voltage ranges, especially as the fit is often applied to a dynamic voltage range close to the SET and RESET.[135,136,140,141,143,146] In this range, the oxygen vacancies migrate and change the conduction. Thus, it is meaningless to consider the electronic transport without taking this into account. Furthermore, the SCLC model is a bulk conduction model. It ignores the influence of the electrodes on the electronic transport. As discussed before, the bulk transport results in a polarity symmetric transport, whereas the transport in VCM cells typically has asymmetric characteristics. Another issue is that the detected power law could be alternatively explained as a slow increasing exponential function. The extraction of the different slopes is thus ambiguous. Furthermore, in the LRS the power law often follows a linear, ohmic like, behavior with $\alpha \approx 1$, which is not consistent with the SCLC model.

In the study of Matveyev et al., the interface limited trap assisted tunneling as suggested in the work Yu et al. has been successfully fitted to the electronic data.[115,120,133] With the same measured data, Matveyev et al. successfully applied the SCLC analysis of a linear fit to a double logarithmic plot. This analysis reveals that the data explained by an interface limited trap assisted tunneling transport mechanism are comparable to the results in Figure 4. Thus, it proves that the trap-assisted tunneling conduction type could be accidently misunderstood as SCLC conduction.

In conclusion, the SCLC cannot be generalized without solving the listed counterarguments and is, therefore, a rather special case of conduction in VCM cells and cannot simply be generalized to the majority of these cells.

C. Poole−Frenkel Conduction. The Poole Frenkel (PF) mechanism is another conduction process based on trap states. In contrast to the TAT model, the trapped electrons do not

https://doi.org/10.1021/acsaelm.1c00398
ACS Appl. Electron. Mater. 2021, 3, 3674−3692

conduct by tunneling between the traps. Instead the electrons are released by a thermal excitation into the conduction band. The electrons are then transported over the conduction band to the electrode. The thermal excitation barrier is determined by the depth of the trap state ϕ_t. The presence of an electric field reduces this barrier due to an image charge effect. The geometrical analysis of this problem leads to a thermal excitation barrier which is reduced by the square root of the electric field. The resulting conductivity is analytically described by

$$\sigma = \sigma_0 \exp\left(-\frac{\phi_t - \sqrt{\frac{e^3}{\varepsilon_0 \varepsilon_r} F}}{k_B T}\right) \quad (2)$$

with the barrier ϕ_t, the conductivity prefactor σ_0, the temperature T, and the Boltzmann constant k_B.[157−159] In the case of a constant electric field, F equals the applied voltage divided by the layer thickness. Thus, $\log(I)$ will become proportional to the square root of the applied voltage. Such a relation was found in $I-V$ curves of the VCM cells, and thus, PF was suggested as the dominating conduction mechanism.[160,161] As this is a bulk transport mechanism, the same problem arises as in the analyses before: i.e., it can hardly explain the asymmetric switching properties of VCM cells. Moreover, the square root dependence on the voltage is only achieved if the voltage drops homogeneously over the oxide layer. It is questionable whether such a basic approximation could be generally assumed for nanoscale devices. In addition, a homogeneous trap density is assumed in eq 2, but the permanent redistribution of oxygen vacancies leads to a gradient in the trap distribution and the electric field. Thus, the assumptions made in the derivation of the PF conduction mechanism are likely to be violated in VCM cells.

A general problem of determining the conduction mechanism is that often only the voltage dependence is considered at room temperature and other parameters like the layer thickness or the temperature dependence are not considered. This problem has been discussed in more detail in the literature.[115,162] Due to the missing double check of other parameters, the PF could be mixed up with another conduction mechanism, which approximately have a square root voltage dependence.

In the work of Matveyev et al.,[133] the authors could reproduce their data using the interface limited trap assisted tunneling. In the previous section a double logarithmic plot shows that the same data could be also displayed in the form of SCLC. In addition, Matveyev at al. apply a PF analysis to the exact same data and reveal that the square root dependence could be successfully applied to the $I-V$ curve. However, when the temperature is varied the data does not follow the PF temperature dependence. This makes the study of Matveyev highly interesting, because the authors showed that the data, which can be consistently explained by an interface limited TAT, can at first glance also be misunderstood as SCLC or PF conduction. Furthermore, it has been shown for thin films that the apparent PF conduction could also be understood as the superposition of other conduction mechanisms.[163]

The above discussion shows that the PF conduction is unlikely to describe the conduction in state-of-the-art VCM cells consistently.

D. Schottky Barrier Limited Transport. In PF conduction, the electrons move within the conduction band, but the conduction is not limited by the band mobility. Instead it is limited by the supply of mobile charge carries, which are trapped in the defect states. The same is true for Schottky contact limited transport, where the supply of charge carriers stems from the electrode and is limited by the amount of electrons that cross the Schottky barrier. In general, a VCM cell has two Schottky contacts at the two metal contacts. However, the conduction limiting Schottky contact is found at the electronically active electrode, where the high metal work-function leads to a high electrostatic barrier. The ohmic electrode typically forms a good conducting contact, which is comparable to the quasi ohmic contact known from highly doped semiconductors. Hence, this contact is in good approximation negligible. Hence, the active Schottky interface must be modulated to invoke the resistive switching. Note that when the Schottky barrier height becomes identical at both sides, the resistive switching shows symmetric complementary resistive switching (CRS) behavior.[129−132]

The Schottky barrier limited transport could be the dominating conduction mechanism in many VCM cells, because it is consistent with the polarity dependence of the $I-V$ characteristic and the polarity dependence of the switching, and it is also consistent with the dependence on the electrode material. Besides these vague arguments, several scientific articles also suggest the Schottky conduction mechanism.[65,164−167] For a detailed understanding, however, it must be explained how the transport across the Schottky barrier arises and how it is modulated by the oxygen vacancies.

In general, the transport at the Schottky contact can be categorized in three subclasses: thermionic emission (TE), field emission (FE), and thermionic field emission (TFE). In the TE scenario, the electrons overcome the Schottky contact by a thermal excitation to energies above the Schottky barrier. FE describes the tunneling from the metal Fermi edge through the full depletion zone into the conduction band of the semiconductor (and vice versa). In this case, no thermal excitation is required. TFE is a mixture of both TE and FE. Here, the electrons tunnel through the Schottky barrier at a higher energy level. At the higher energy level, the electrons benefit from a shorter tunneling distance and a smaller tunneling barrier compared to FE. On the other hand, this requires a thermal excitation. Hence, TFE is a balance between enhanced tunneling probability and reduced thermal excitation probability.

For all three subclasses, analytical equations have been derived.[168,169] In the case of TE, the forward direction of the Schottky diode shifts the conduction band upward and effectively reduces the thermal excitation barrier, which leads to an exponential current−voltage dependence proportional to $\exp\left(-\frac{eV}{k_B T}\right)$. For the reverse direction, the excitation barrier is reduced due to the image charged barrier lowering as in in PF conduction. This results in an exponential dependence on the square root of the voltage. In both cases, a thermal excitation is required, which is typically described by the Boltzmann approximation of the Fermi distribution.

The most popular equation for FE has been derived on the basis of the work of Fowler and Nordheim.[170] Here, the Wentzel−Kramers−Brillouin approximation is applied in the model to calculate the tunneling probability through the Schottky barrier.[171,172] This equation is temperature inde-

https://doi.org/10.1021/acsaelm.1c00398
ACS Appl. Electron. Mater. 2021, 3, 3674−3692

pendent due to the direct tunneling but has an exponential current voltage dependence, as the Schottky barrier and tunneling distance change under the voltage stress.

For the TFE, an analytical equation has been derived by Padovani and Stratton.[169] They developed the model under the condition that the tunneling occurs mostly at one specific energy level, which depends on the Schottky contact properties. At this energy level, the tunneling probability is combined with the thermal excitation probability based on the Boltzmann approximation. As a result, also this conduction mechanism has an exponential voltage dependence, for the same reasons as FE and TE. For the same reason, TFE is also polarity dependent.

These analytical equations are applied to detect the conduction subclass for the specific Schottky contact system. To this end, the voltage dependence of the analytical equations are compared to the measured $I-V$ curves. This is, however, a critical point as these equations are initially derived for typical covalent semiconductors, e.g. silicon. In contrast, VCM cells are constructed out of an oxide with a much wider band gap. Additionally, the already mentioned shortcoming of nonhomogeneous and variable doping concentrations based on crystal defects is another issue in this fitting analysis. Furthermore, all types of conduction have an exponential voltage dependence. Thus, the same curve may be fitted assuming any of the TE, FE, and TFE models if the parameters are freely chosen. Hence, it is important to check whether all fit parameters are physically meaningful and reasonable in the context of VCM cells. As mentioned before, a second test of other parameters like temperature, metal electrode, or, if possible, the doping concentration should be used to double check the conclusion. Those parameter changes should follow the predictions given in the analytical equations.

A possible procedure to verify the conduction mechanism is to extract one parameter by fitting the $I-V$ curve and use a second independent experiment to verify this parameter. This approach has been applied by Lee et al.[173] They extracted the Schottky barrier height for the HRS and the LRS using a TE fit. The fitting suggests a smaller Schottky barrier in the LRS (≈0.75 eV at 1 V) than for the HRS (≈0.88 eV at 1 V). In consequence, they suggest that the resistive switching is an effect of modifying the Schottky barrier height due to the amount of oxygen vacancies. This is a realistic approach due to the Schottky barrier lowering effect, which could also be initiated by oxygen vacancies.[174] The part, which makes the work of Lee et al. outstanding, is the second experiment based on internal photo-emission spectroscopy (IPES). They extracted the Schottky barrier height from the IPES measurements, but the extracted values did not match the fitted Schottky barrier values. The IPES values are clearly higher and located slightly above 1.1 eV at 1 V. Another inconsistency is that the Schottky barriers in the IPES barriers are equal for LRS and HRS. The solution to this inconsistency as suggested by Lee et al. is a parallel conduction path, meaning that in a tiny local range the Schottky barrier is lowered to the LRS and HRS values. This small range dominates the current transport, but the IPES measurements reveal the average Schottky barrier height. This solution makes sense, but this extra path could also have other causes, for instance a TFE conduction, where the tunneling occurs at this specific energy. This option has been tested using ab initio simulations in our previous work,[162] which will be reviewed in the discussion part. Using such a kind of ab initio simulations has the advantage that it requires less approximations and assumptions than in the analytical ansatz. The disadvantage of this approach is the high computational costs, which limits the simulated cell size to a few atoms, much less than in real systems.

COMPREHENSIVE MODEL OF THE ELECTRON CONDUCTION AND SWITCHING MECHANISM

As outlined in the previous section, using text book analytical equations to identify the conduction mechanism of VCM cells has several pitfalls. Quite often the underlying assumptions are violated as the oxygen vacancy concentration is nonhomogeneous and varies during switching in VCM cells. In addition, the total conduction may be limited by different conduction mechanisms depending on the applied voltage regime. Thus, a more sophisticated modeling approach considering the oxygen defect distribution is required. As shown in Figure 1, the majority of the VCM devices can be categorized in two type of $I-V$ curves: a highly nonlinear asymmetric type (type 1) and a more linear type (type 2).

Type 1 $I-V$ Characteristics. In our previous studies, we investigated type 1 conduction with a strong exponential $I-V$ curve, using density functional theory combined with the nonequilibrium Green's function formalism (DFT + NEGF) as implemented in the Atomistic Tool Kit (ATK).[175,176] As exemplary system for the type 1 $I-V$ curve, we investigated a $Pt/SrTiO_3$ based VCM cell.[162] Figure 5a shows the atomistic model of the $Pt/SrTiO_3$ supercell. The $SrTiO_3$ slab contains one oxygen vacancy, which corresponds approximately to a vacancy concentration of 5×10^{26} m^{-3}. The results have been published in our previous work[162] and are reproduced using a later version of the simulation program ATK. (The possible influence of the $Nb:SrTiO_3$ ohmic electrode has been verified in another work[177] and leads to the same conclusions.) A useful tool to visualize the electronic structure is the local density of states (LDOS), which delivers an energy and space resolution of the electronic states. This LDOS has been plotted for three different voltages in Figure 5b. The different voltages lead to a separation of the quasi Fermi level and shifts the metal Fermi level to higher energies. The color map reveals many electronic states at energies and positions with a bright purple color. In contrast, the dark regions in the LDOS have zero electronic states. The simulated LDOS could be understood as follows: On the right side many purple states are found at the Fermi level and over the full energy range, which represents the metallic character of the Pt electrode. In the $SrTiO_3$ part, a dark region forms around the left quasi Fermi level, which indicates that no electronic states are found at this energy. This missing of states represents the band gap of the $SrTiO_3$. The bright purple regions energetically below and above the left Fermi level are the valence and conduction band, respectively. Hence, the conduction band minimum (CBM), as the most important ingredient for the band transport, could be traced by using the LDOS. The CBM is the upper transition line between the bright purple region and the dark region in the $SrTiO_3$ slab and marked by a white line. The conduction band shows an upward bending toward the Pt contact, which results in the Schottky barrier. The applied voltage corresponds to a reverse bias Schottky contact, which becomes visible in the LDOS by the increased band bending. To analyze the current transport, the NEGF mechanism is used to calculate the spectral current as it is defined by Stradi et al.[176] The spectral current is an energy-resolved current, which indicates the current transport in each energy range and is plotted for the

https://doi.org/10.1021/acsaelm.1c00398
ACS Appl. Electron. Mater. 2021, 3, 3674−3692

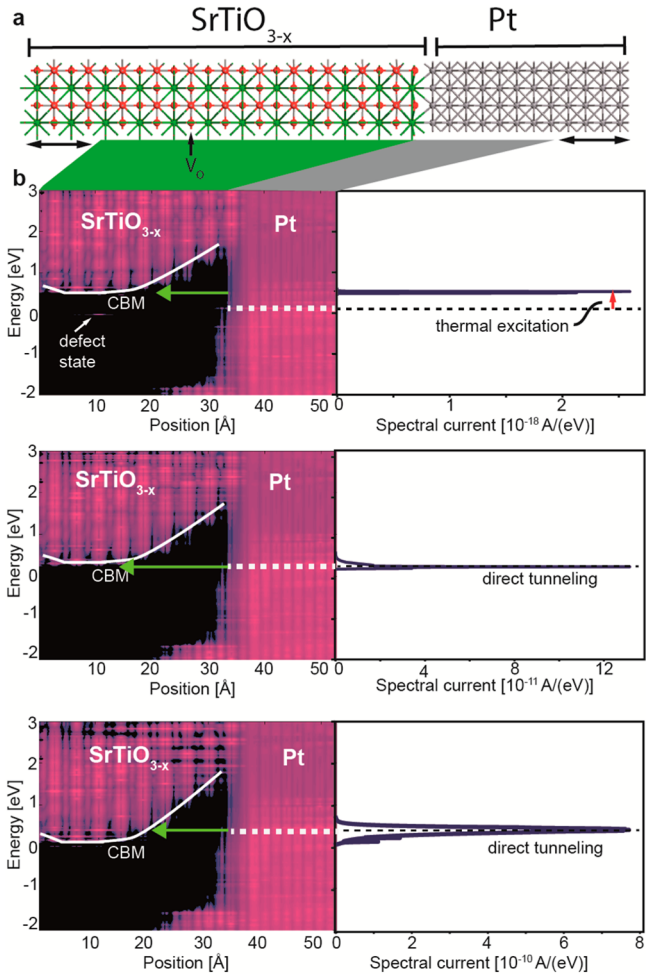

Figure 5. (a) Supercell for the DFT + NEGF simulations of the $SrTiO_3$/Pt Schottky, as used in our previous work.[174] The arrow at the V_O shows the position of the oxygen vacancy in the $SrTiO_3$ slab of the super cell. The double arrows are the simulation boundary conditions specified in the Methods section. (b) LDOS at 0.1 V (top), 0.6 V (middle), and 0.9 V (bottom). The right side shows the calculated energetically resolved current spectrum, compared to the LDOS. The white line is the conduction band minimum (CBM), and the dashed line is the quasi-Fermi-level in the Pt electrode.

three voltages in Figure 5b. For all voltages, the spectral current has a peak-shaped distribution with a maximum lower than the Schottky barrier height but higher than the CBM minimum. Hence, the quantum mechanical simulations suggest a tunneling through the Schottky barrier into the conduction band. At lower voltages, the peak of the spectral current is higher than the Fermi level of the right electrode and the electron tunneling requires a thermal excitation to this energy level. At higher voltages, the electrons can tunnel directly from the Fermi edge, which leads to a direct tunneling transport.[100,162] This results in a special transition from thermally excited to direct tunneling. Experimentally, this transition has been verified by electrical characterizations at different temperatures T. At the transition from thermally excited to a direct tunneling, the temperature dependence changes.[162] This principle of conduction has been verified for several resistance states (differing by many orders of resistance) using experimental electrical characterization of the $SrTiO_3$/Pt systems. In addition, the atomistic model shows consistent results with a continuum simulation model implementing the atomistic conduction picture.[100] Using this continuum model, the experimental current transport for the forward direction has been correctly predicted. This shows that the proposed conduction model consistently explains the forward and backward direction conduction of the $SrTiO_3$/Pt system including a change in the temperature dependence at high voltages.[76,100,162] The consistent description of the experimental data with this model suggests a conduction mechanism based on a band transport, which is limited by the electron transfer across the active Schottky contact. The huge exponential character stems from the thermal activation and the reduction of the tunneling distance through the Schottky contact barrier. The resistive switching behavior is invoked by changing the oxygen vacancy concentration at the Pt interface, which shortens and widens the tunneling distance at the interface by changing the Schottky screening length. In conclusion, the presented results are consistent with the facts of a strong exponential voltage dependence and the known influence of the metal electrodes. This conduction mechanism has been also successfully applied to a VCM system based on TiO_2.[68] Furthermore, it is consistent with the dynamic continuum simulations in refs 178 and 179 which apply a band conduction model with two Schottky barriers.

From this point of view, it is likely that this type of conduction could be generalized to systems with a strong exponential voltage dependence. Hence, the type 1 conduction mechanism is a band transport, which is limited by the Schottky contact at the electronically active electrode. The exact coupling between the metal contact and the oxide conduction band may differ depending on the VCM system. Depending on the metal/oxide interface, the transport across the Schottky contact could have different origins: thermionic emission, thermionic field emission, and field emission. However, the identification of the conduction mechanism by fitting an analytical equation should be checked carefully. As discussed before, the analytical equations are derived under conditions, which are unlikely to be found in VCM cells, such as a precise homogeneous doping distribution generated under laboratory conditions.

Theoretically, the thermionic emission as a transport over the barrier is possible. In a degenerated semiconductor/insulator also field emission may become possible. The quantum mechanical simulations suggest a tunneling process and it is likely that this is also valid in most type 1 VCM systems. Note that the simulations contain all energy contributions and could lead to any kind of transport across the barrier, namely TE, TFE, and FE. The argument is that type 1 VCM systems exhibit high Schottky barriers. Additionally, the thin layer oxides are only a few nanometers, which means that the screening length must be very short in order to allow a change in the conduction by a change in the oxygen vacancy concentration. Thus, a tunneling process is very likely to happen for these systems. Nevertheless, it depends on the specific system in which the Schottky contact is overcome, but all fall into the category of conduction band transport.

Type 2 *I*–*V* Characteristics. Now, we apply the DFT + NEGF method to a system with type 2 I–V characteristics showing less nonlinear behavior. To this end, a supercell is generated, which represents a Ti/HfO_2/Pt layer stack. In this case, the electronically active electrode is the Pt electrode. The supercell is plotted in Figure 6a and has an HfO_2 layer thickness of 3 nm. The HfO_2 layer is divided into three zones of 1 nm, which are differently colored. To realize different

https://doi.org/10.1021/acsaelm.1c00398
ACS Appl. Electron. Mater. 2021, 3, 3674−3692

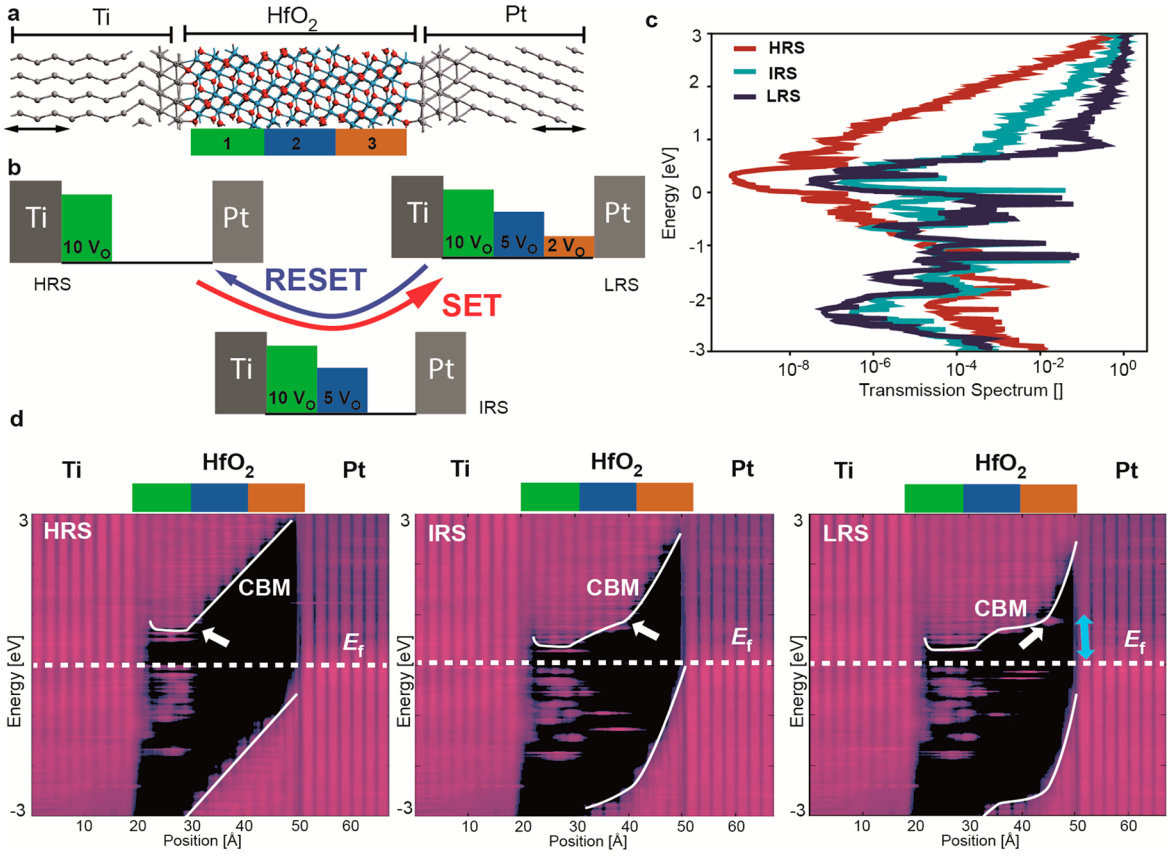

Figure 6. (a) Supercell of the HfO_2 based Ti/HfO_2/Pt VCM cell. The simulation boundary conditions specified in the Methods section are marked by the double arrow. The HfO_2 has a thickness of 3 nm. (b) Sketch of the realization of the resistance states. The colors correspond to the regions in supercell a. (c) Transmission probability of the three different atomic configurations (HRS, IRS, LRS). (d) LDOS of the three different resistance states at zero voltage. The white lines are the CBM and VBM. The dashed line is the Fermi level. The white arrow marks the screening kink in the CBM. In the LDOS of the LRS, the blue double arrow indicates the thermal excitation to the defect state that is nearest to the Pt interface.

resistance states, different numbers of oxygen vacancies are inserted into these zones. To represent the HRS, ten oxygen vacancies are inserted into the first 1 nm zone directly at the Ti interface. This leads to a 2 nm gap without any oxygen vacancies at the active electrode. For the intermediate state (IRS), five further oxygen vacancies in the second 1 nm range are added to the HRS configuration. This leads to an oxygen vacancy free gap of 1 nm at the active electrode. For the LRS, two additional oxygen vacancies are inserted in the third 1 nm range close to the active electrode. This closes the gap at the active electrode. To illustrate the closing of the gap, the HRS, LRS, and IRS are sketched in Figure 6b. In general, the oxygen vacancy concentration is not constant during switching, which requires an oxygen exchange with the environment/electrodes. Nevertheless, a comparable scenario in which the amount of oxygen is conserved could be created. To this end, the oxygen vacancy reservoir at the Ti electrode is partly depleted by displacing oxygen vacancies to the gap region close to the active Pt electrode. The concentration gradient in this scenario is approximated by three ranges of decreasing amount of oxygen vacancies. Dividing the structure into more ranges is limited due to the limited size of the supercell of a few hundred atoms in our ab initio simulations. The conclusions, however, remain valid for another choice of gradient.

For the three described atomic configurations, the transmission spectrum and the LDOS are calculated by means of DFT + NEGF. The transmission spectra of all structures have a comparable character and are plotted in Figure 6c. They show a transmission above 0.6 eV, which corresponds to a transport over the conduction band of the HfO_2. In the energy range below 0.6 eV, the transmission spectrum has several peaks which originate from the transport via the defect states induced by the oxygen vacancies.

The LDOS of the HRS is plotted in Figure 6d. It reveals the metal insulator metal structure. At the left Ti metal electrode, many electronic states over the whole energy range exist. The same applies for the Pt electrode on the right side. Both metals have a different work function, which is compensated by a charge transfer. This effect shows in the LDOS by a bending of the conduction band. Again, the transition line between the bright and dark region in the HfO_2 range of the LDOS defines the CBM, which reveals the expected band banding. In a perfect insulator, the conduction and valence bands form a tilted rectangle, because no screening is possible due to the low charge in the insulator. Here, the depicted scenario clearly differs from the tilted rectangle, because of the oxygen vacancies, which disturb the perfect insulating character. The oxygen vacancies induce a defect state in the band gap. This generates a bright purple spot within the simulated LDOS of the HfO_2 band gap. In the HRS configuration, a huge accumulation of oxygen vacancies close to the Ti electrode leads to overlapping defect states. As a consequence, the defect states distribute over an energy range, which suggests a subband formation. In the LDOS, this leads to the purple range in

https://doi.org/10.1021/acsaelm.1c00398
ACS Appl. Electron. Mater. 2021, 3, 3674−3692

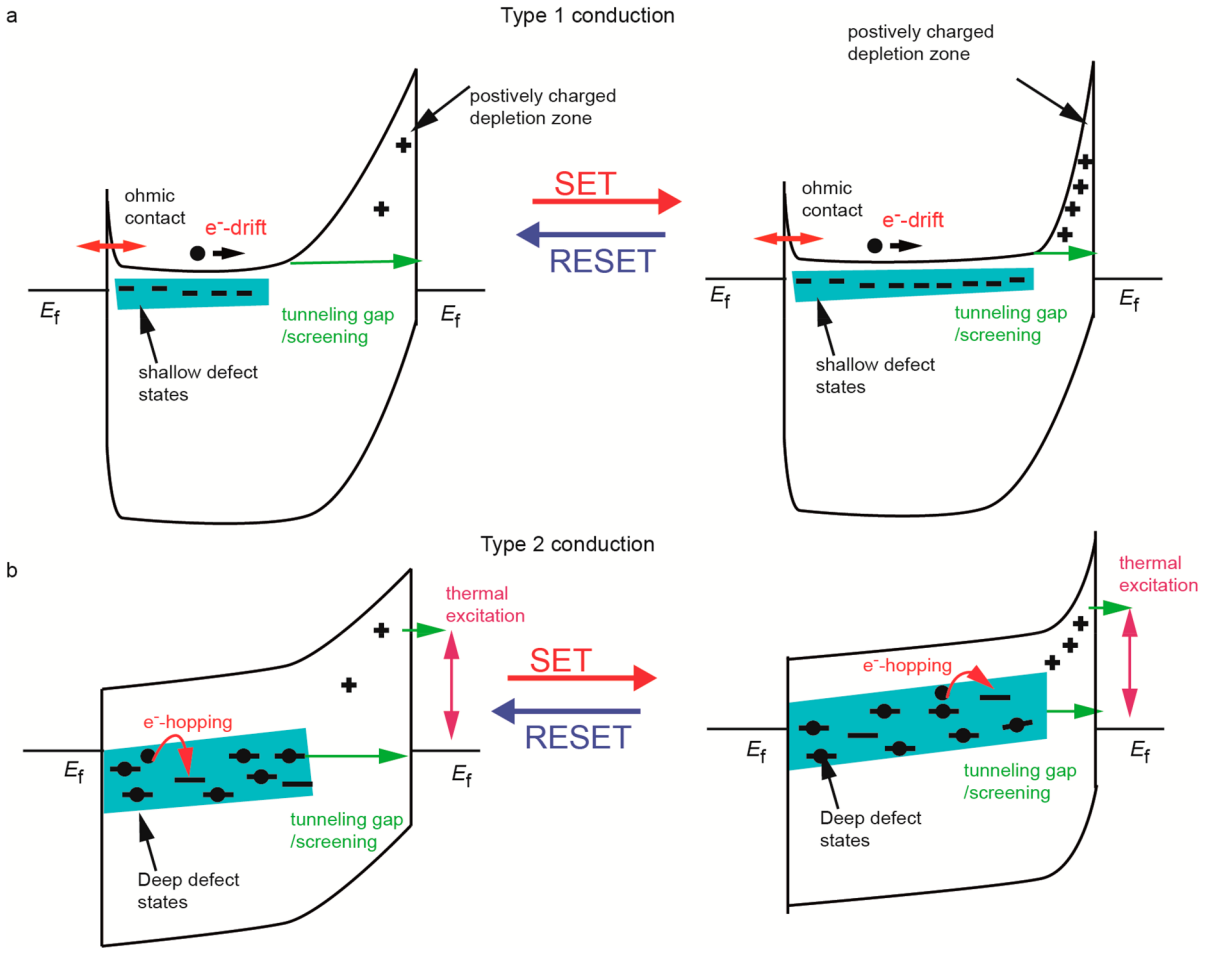

Figure 7. Sketch of the band diagrams for the HRS (left) and LRS (right) conduction in (a) type 1 and (b) type 2 devices under a small read voltage. The defect states are induced by oxygen vacancies. The gray region indicates that the defect states might be smeared over a certain energy range. The SET/RESET switching occurs due to a reconfiguration of the oxygen vacancies.

the first 1 nm zone. At the position of the high oxygen vacancy concentration, the conduction band shows a kink, which stems from the screening of the Schottky interface.

The intermediate state has five additional vacancies in the middle range, which reduces the vacancy free gap to 1 nm. Again, looking at the defect states, five additional purple spots arise from these oxygen vacancies, but the tendency towards sub-band formation is reduced. As a result, the screening already occurs in the middle of the device and the kink shifts into the second 1 nm zone. This effect further enhances in the LRS configuration, where the two additional oxygen vacancies are inserted into the third zone. Here, the Schottky barrier screening is shifted toward zone 3 and the kink is found closer to the active Pt electrode. In conclusion, in all cases the simulation results suggest a trap-assisted tunneling transport due to the peaks in the transmission spectrum (cf. Figure 6c) at the energy levels of the defect states. On average, the transmission increases from the HRS to the LRS as the "gap" closes and the transmission probability of electrons through the gap increases. This trap-based transport is in accordance to many other studies as discussed before. It also includes the studies, which suggest a space charge limited current transport, where the conduction in the HfO_2 layer is determined by a trap-to-trap transport. The electrode interface, however, has a strong and important influence, which contradicts the trap-based models that only consider the bulk transport. This issue has been addressed in the highly relevant study of Yu et al., in which an interface limited trap assisted tunneling is proposed.[120] In this study, the random telegraph noise (RTN) of four different resistance states is analyzed by extracting the power spectral density. The analysis suggests a tunneling from the electrode to the nearest trap (induced by an oxygen vacancy defect state) as limiting conduction mechanism. In the HRS, a gap without any oxygen vacancies arises at the active electrode. In this case, the interface nearest trap limits the tunneling into the Pt electrode. In the LRS, this gap is closed and many trap states are close to the interface. Therefore, the tunneling between electrode and trap occurs over many defect states. The transport within the oxide in this model occurs over the trap states induced by the oxygen vacancies. This could be either a trap-to-trap tunneling or a sub-band transport. The limiting step determining the overall resistance is the tunneling between trap and metal electrode. The switching is then based on the reduction of the tunneling distance between traps and interface. In the study of Yu, however, space charges or the difference in the metal work function is neglected. The latter changes the energetic position of the defect states. Consequently, the defect states are not aligned to the Fermi level and a direct tunneling is not possible. This alignment of the defect states is also not generally valid. The position of the defect states depends on the used materials, which would also prevent a direct tunneling.

https://doi.org/10.1021/acsaelm.1c00398
ACS Appl. Electron. Mater. 2021, 3, 3674−3692

Therefore, the model of Yu should be extended by considering the DFT + NEGF results, which reveal the relevance of space charge. Our DFT + NEGF simulations reveal that the direct tunneling from the Fermi edge could only occur to the defect positions at the end of the Schottky barrier depletion zone. The reason for this is that at this position the traps are pinned to the same energetic position as the Fermi level. The oxygen vacancy, which is closest to the electrode is at a higher energy level above the Fermi level. Consequently, a thermal excitation is required for this tunneling process. Hence, there are more opportunities to overcome the Schottky interface: (1) a thermally excited tunneling into the interface nearest trap; (2) a direct tunneling into the trap states near the Fermi edge at the end of the depletion zone. Whether case 1 or 2 is the dominating one depends on the thermal excitation probability with respect to the tunneling probability through the depletion zone. In the LDOS's of Figure 6d, this tunneling would require a thermal excitation of about 1 eV. At room temperature, the Fermi distribution lowers by more than 15 orders of magnitude. This 15 orders of magnitude must be compared to the benefit of a shorter tunneling distance. To this end, the variation of the transmission spectrum in Figure 6c can be used, which only shows a change of about 6 orders of magnitude. Thus, it is clear that the required thermal excitation probability could not be compensated by the shorter tunneling distance. As a result, the dominating charge transfer at the interface is given by process 2 of direct trap to electrode tunneling.

In conclusion, the interface limited direct tunneling into the trap states as explained by Yu gives, in general, the correct picture, but the tunneling distance is not determined by the interface nearest trap state. Instead, the tunneling distance is determined by the Schottky screening distance, which is the position of the kink in the LDOS states. At this screening distance, the trap states are located at the Fermi level. The resistive switching effect is thereby invoked by a change of the tunneling distance which is determined by the oxygen vacancy defect concentration. In the HRS, the screening distance is long and for the LRS the screening distance becomes short. To conclude, the screening distance replaces the trap to interface distance in the interface-limited TAT model.

DISCUSSION

Based on the DFT-NEGF simulations of a $Pt/SrTiO_3$ VCM system and a $Pt/HfO_2/Ti$ VCM cell, we identified two different type of conduction mechanism. Figure 7 illustrates the conduction mechanism for the LRS and the HRS for both systems. While the details of the conduction mechanisms are different, the broader picture of the switching and conduction mechanism are very similar. For both systems, the HRS state is described by an oxygen vacancy rich range at the ohmic electrode and an oxygen vacancy depleted zone at the electronically active Pt electrode. The Schottky contact at the Pt electrode is screened at the trap rich region, which is the kink in the CBM in the LDOS of the DFT + NEGF simulations (cf. Figure 6d). One effect of this screening is that the Fermi level is pinned at the defect state level in the oxygen vacancy rich region. The resulting Schottky barrier at the Pt/oxide interface limits the conduction in both cases. Due to the different defect levels in the two systems, however, the electrons are transported at a different energetic level. For the $Pt/SrTiO_3$ system, the defect states are rather shallow, which allows a tunneling transport between the Pt electrode and the conduction band of the $SrTiO_3$. The electrons are then transported via the conduction band. In the $Pt/HfO_2/Ti$ system, in contrast, the electrons tunnel from the Fermi edge in the metal to the "deep" defect states within the band gap. The electrons are then further transported via the traps in the oxides, which could in principle also form a sub-band. An important result is that the tunneling distance in both cases is determined by the screening length of the Schottky depletion zone, but not by the distance to the nearest oxygen vacancy. The oxygen vacancy defect states in this depletion zone are positively charged and located above the Fermi level as typical for *n*-type Schottky contacts.

The two different conduction paths (via the conduction band and via the traps) lead to two different shapes of the barrier. In the case of the tunneling into the conduction band, a "triangular" (or parabolic) barrier results comparable to the Fowler–Nordheim case. Thus, if a voltage is applied the effective tunneling distance decreases and an exponential $I-V$ relation results. In addition, a pronounced asymmetry with respect to the voltage polarity is expected. In the $Pt/HfO_2/Ti$ system, in contrast, the electrons tunnel mainly at the Fermi edge in a quite narrow energy range. The form of the barrier can be thus be better approximated as an asymmetric trapezoidal barrier as described by Simmons.[180] In this case, the effective tunneling distance remains constant as long as the applied voltage is not too high. This would result in a more linear and more symmetric $I-V$ curve. Nevertheless, the height of the electrostatic barrier is reduced in both cases by image force barrier lowering. This will impact mainly the transmission probability and will also lead to a voltage dependence. This voltage dependence, however, is less pronounced as in the case of the voltage dependent reduction of the tunneling distance. The same considerations are valid for the LRS. The major difference in the LRS is that the oxygen vacancy concentration at the interface is higher in the LRS, which reduces the screening distance. As a result, the direct tunneling distance is reduced. This leads to a lot higher current. In the same way, intermediate resistance states are described by different screening length often interpreted as different gap size. This means that the conduction mechanism does not change; thus, the main characteristic of type 1 or type 2 conduction are preserved. For very thin barriers (or low barriers with low work function metal), however, the interface limited transport and the bulk transport (via trap levels or the conduction band) can become comparable. In the case of the $Pt/SrTiO_3$ system, this leads to a change in the limiting transport mechanism at higher voltages. At low voltages the interfaces is limiting, but at high voltages the bulk part becomes limiting. This transition manifests in a change of the temperature dependence of the current transport as discussed before.[100] The intermediate resistance states could be implemented by different current compliance or a current limiting serial resistance.[181] This leads to different ionic concentrations or a different balance between bulk and interface transport. Therefore, the shape of the $I-V$ characteristic modifies slightly, but it is not expected to change the fundamental properties such that it lead to a swap between type 1 and 2. Other geometrical aspects as the diameter of the filament shifts the current level but does not change the current voltage dependence.

To summarize, the origin of resistive switching mechanism is identical for both type of conduction. The Schottky depletion zone is modified, but the tunneling process is different. For both systems the resistance state is determined by the

https://doi.org/10.1021/acsaelm.1c00398
ACS Appl. Electron. Mater. 2021, 3, 3674–3692

distribution of the oxygen vacancies. They will determine the shape, i.e. the height and distance, of the Schottky barrier. As typically two different metals with different work functions are used, the initial shape of the electrostatic barrier is different and one barrier will dominate. Thus, the change of the oxygen vacancy concentration at the wider and higher barrier (i.e., close to the higher work function metal) determines the resistance state of the device. A high concentration leads to a low resistive state, whereas a low concentration leads to a high resistive state. This explains the clear bipolar switching behavior of VCM cells. The resistive switching is induced by changing the amount of defects close to the electronically active electrode. This can be accomplished in two ways. In the first scenario, the oxygen vacancies are redistributed by ion migration within the oxide including possible oxygen exchange reactions at the ohmic electrode. In this case a so-called counter-eightwise switching is observed.[182,183] This means that the device sets/resets with a negative/positive voltage applied to the electronically active electrode. In the second scenario, the oxygen vacancy concentration changes due to an oxygen exchange at the electronically active electrode. This results in the opposite switching polarity also called eightwise switching.[67] The SET/RESET process occurs by applying a positive/negative voltage to the electronically active electrode. In fact, both processes can occur in parallel depending on the specific VCM cell. It has been even shown that both switching polarities can appear in the same cell.[68,184−186]

From this point of view the model for the conduction mechanism reveals that the ion dynamics must lead to a modification of the electron transport through the active electrode/oxide interface. The conduction model does not explain the dynamics of the resistive switching. However, it is clear that ion dynamics and electronic conduction are strongly correlated. As described in the dynamic model of Marchewka et al.,[178] the ion transport and thus the switching dynamics are influenced by the local electric field and the local temperature. Both quantities are influenced by the conduction mechanism. The electric field is the driving force for the ion transport. As the current transport due to the ions is small compared to the electronic contribution, the local electric field is defined by the electrical current. From the here presented model one can conclude that the applied voltage drops mainly over the depletion region. Hence, at this position the modification of the electric field is significant. Moreover, the change of the size of the depletion region will have a significant impact on the electric field and thus the driving force of the ion motion. It should be noted that for high voltages a significant voltage drop will occur also over the "bulk" of the oxide. This inhomogeneous and voltage-dependent local field distribution, which is a result of the proposed conduction mechanism, will significantly influence the local ion transport and, in turn, the switching dynamics. The second important parameter is the temperature, as this enhances the ion hopping transport of the oxygen. Menzel et al.[187] showed that a local temperature increase in a filamentary region explains the strong nonlinearity of the switching dynamics. The origin of this temperature increase is the Joule heating, which is also determined by the conduction mechanism. Due to the voltage drop at the interface it is likely that the Joule heating at the active electrode is the highest, but due to the small dimensions of the filaments the Joule heating could also arise further away from the interface. An important aspect is that the nonlinearity of the $I-V$ curve will also influence the switching dynamics if Joule heating occurs. For a linear $I-V$ curve, the dissipated power increases quadratically with the applied voltage. In contrast, for an exponential $I-V$ curve, the dissipated power also increases exponentially. This can lead to a high nonlinearity of the switching kinetics.

The two investigated model systems can represent the two different type of $I-V$ curves. The main difference of these two systems is the type of the defect states. In case of the Pt/$SrTiO_3$, the defect level induced by the oxygen vacancy is shallow and a type 1 conduction appears. In contrast, the defect level lies deep in the band gap in the HfO_2 system and a type 2 conduction results. Thus, we propose that the type of defect determines the type of conduction. If the oxygen vacancies induce shallow defect levels, type 1 curves result. In contrast, a type 2 curve is obtained if the oxygen vacancies induce deep defect levels. Linderälv et al.[101] investigated oxygen vacancies in several oxides using the hybrid functional DFT method. They demonstrated that all oxygen vacancy states are found in a tiny energy range compared to the vacuum energy level. Within this arrangement it is possible to distinguish two type of defect states. One type has a deep donor like defect level, and the other forms a shallow defect state. These two types differ also in the shape of their eigenstate. The deep levels form an s-type defect state and the shallow level a p-type state. This category fits to our analysis for the two type of conduction mechanism. Linderälv et al. reported shallow defects levels for TiO_2, which shows a strong exponential type 1 $I-V$ curve when used in a VCM cell. For $SrTiO_3$ also shallow defect state with the same p-type eigenstate are reported independently[188,189] For HfO_2, Linderälv et al. report a deep defect state, which will lead to the interface-limited trap-based transport, which should show a more linear type 2 conduction. This fits to the experimental observation of type 1 and type 2 conduction in these materials.[83,88,94,95]

In the Introduction we presented some examples from the literature for type 1 and type 2 of the conduction mechanism for VCM cells based on different oxides. A couple of them have been considered in the work of Linderälv, which are categorized into shallow and deep oxygen vacancy level. Hence, for these materials the required data are available to prove the hypothesis. For the materials $BaTiO_3$, In_2O_3, and Sn_2O_3, a more shallow defect state is reported. The $I-V$ curves coincide with the type 1 conduction. In contrast, Linderälv et al. found the deep level type of oxygen vacancies in HfO_2, ZrO_2, and Lu_2O_3. In the examples of the Introduction, these two materials led to the second type of interface limited trap assisted tunneling. Consequently, the literature review is consistent with this hypothesis.

From this analysis it is possible to predict the temperature dependence of the two conduction mechanisms. For the type 1 conduction thermal excitation is required, which leads to Boltzmann like temperature activated transport. This has been experimentally confirmed.[76,162,190,191] Only in the extreme case when the insulator becomes degenerated is direct tunneling possible. It is assumed that this is the majority as even shallow defect states are more than 0.15 meV below the conduction band, such that not all donors (vacancies) are activated. For the type 2 conduction, the tunneling occurs into the defect, and mostly to those at the end of the screening length. These, defects are located at the Fermi level and allow a direct tunneling. Hence, only a weak temperature dependence is expected, because most of the tunneling occurs without

https://doi.org/10.1021/acsaelm.1c00398
ACS Appl. Electron. Mater. 2021, 3, 3674−3692

additional thermal excitation. However, a temperature increase could lead to an easier access to defect states, which are slightly above the Fermi level. As a result, a reduced temperature activated transport could be possible, which is also found in lHfO$_2$-based devices.[115,192] For TaO$_x$ as a representative material for the type 2 conduction, the reported temperature dependence is also comparably small[111,193] as expected from our theory.

In the literature, often the temperature dependence is not considered when the conduction mechanism is determined. Consequently, the insufficient data does not allow a final proof of this hypothesis and require further investigations. Nevertheless, the mentioned studies support our hypothesis.

The postulated hypothesis relates the observed experimental characteristics to the nature of the oxygen vacancy defect states, a microscopic property. This offers the perspective of VCM cell design by microscopic considerations. To obtain a highly nonlinear $I-V$ curve a material with a shallow oxygen vacancy defect level needs to be chosen. In case a more linear $I-V$ curve is desired, an oxide material with a deep oxygen defect level needs to be chosen. In addition, the work functions of the two oxides need to be considered as they define the height of the barriers, and thus, the current level. For the target application as an analog synapse in an artificial neural network, a VCM cell with a high resistance tuning range with quasi-analog states is preferred. A high resistance ratio is obtained for type 1 devices as the highly nonlinear $I-V$ curve allows for tuning the device resistance in a large range. It should be noted that a too high nonlinearity could lead to issues during the training procedure. Type 2 devices, in contrast, offer a more linear $I-V$ and could lead to a better training efficiency. As the electron transport in the bulk goes via the trap levels, current jumps will occur due to ion jumps. This has been observed for different type 2 devices.[71,194−196] Thus, it becomes hard to program clearly distinguishable multilevel states. The above considerations are rather general. For a specific application, the trade-off between the desired properties and the available choice of materials need to be considered. One additional aspect is the programming capability of the different VCM cells. If a certain device stack offers the optimal resistance tuning properties but can only be programmed with very high voltages, it might still not be usable for a specific application.

CONCLUSION

In this article, we discussed the conduction mechanism of VCM type memristive devices. In general, one can distinguish two major types of $I-V$ curves, as shown for the SrTiO$_3$/Pt and HfO$_2$/Pt systems. The SrTiO$_3$ based cell has a strong exponential $I-V$ characteristic, and the HfO$_2$ based cell has a much reduced strength in the $I-V$ characteristic. In the literature, several conduction mechanisms for VCM cells have been proposed. A review of these studies reveals some pitfalls when applying text-book conduction mechanisms to VCM cells. In general, the bulk transport mechanism neglects the clear polarity dependence of the VCM switching. In addition, the analytical equations describing these transport mechanisms considers homogeneous properties of the oxide such as a homogeneous distribution of oxygen vacancies. This assumption, however, is not valid for VCM cells as they rely on the redistribution of oxygen vacancies. Thus, the VCM cell needs to be split at least into different regions with different concentrations. In addition, bulk conduction mechanisms neglect the influence of the metal/insulator interfaces. While this may be true for very thick oxides, it is a critical assumption for the typically very thin oxides of a few nanometers in state-of-the-art VCM cells. Electrode limited transport mechanisms can explain the polarity dependence and are therefore highly interesting for a wide class of VCM cells. However, the analytical equations describing the current transport are derived under conditions, which cannot be ensured in VCM cells and, thus, need to be used with care. Nevertheless, the interface-limited trap assisted tunneling conduction mechanism and the Schottky barrier limited band transport mechanism are promising approaches to describe the electron conduction in VCM cells. Using DFT + NEGF simulations, we investigated the two different systems representing the two major $I-V$ curves: a SrTiO$_3$/Pt based VCM cell and a HfO$_2$/Pt cell.

The ab initio simulation of the former system reveals a thermally assisted tunneling, through the full Schottky depletion zone into the conduction band. This fits with the first type of conduction, because it confirms the strong exponential $I-V$ dependence. In the HfO$_2$/Pt based VCM cell, we found indications of an interface-limited transport via the defect states of the oxygen vacancies. This explanation of transport fits with the second type of $I-V$ curve. In both cases, the electron transport is limited by tunneling through the Schottky barrier that forms at the electronically active interface. The Schottky depletion zone determines the tunneling distance, and therefore, the resistance. The resistive switching is then invoked by changing the oxygen vacancy concentration close to this electrode, which modifies the Schottky depletion zone. Finally, we propose a microscopic property that defines the type of conduction: the energy level of the defect state induced by the oxygen vacancy. Oxides with a shallow defect state show a Schottky barrier limited band transport, while deep defects result in an interface limited trap assisted tunneling mechanism. Still, additional work is required to confirm this hypothesis. Nevertheless, this microscopic picture offers a rational design of VCM cells for memory and neuromorphic applications by basic material properties.

METHODS

The simulations are applied using a simulation package (ATK 2018). All structures are relaxed until the forces are below 0.05 eV/Å, thereby the volumes of the electrodes have been constrained. The simulations are applied using the Perdew−Burke−Ernzerhof (PBE) exchange correlation function. Additionally norm-conserving pseudopotentials are applied[197,198] as well as single-ζ basis set plus polarization, as implemented in ATK. For the DFT + NEGF simulations, semi-periodic boundary conditions are applied, called left and right electrode. In the supercell plot those electrodes are signed by double arrows. For the HfO$_2$ simulations, a Monkhost k-point sampling of 3 × 3 × 1 is used in the central device (without electrodes). The same k-point sampling is used for the nontransport directions in the DFT. The density mesh cutoff is chosen to 60 Ha.

The experimental measurements on the SrTiO$_3$ based cell are explained in ref 100, and the fabrication process is detailed in ref 199.

The experimental measurements on the HfO$_2$ based cell have been conducted using an Agilent B1500A Semiconductor Analyzer. The VCM cell is structured as 100 nm × 100 nm on a silicon substrate with a 30 nm thick Pt bottom electrode. The active HfO$_2$ layer has been deposited by atomic layer deposition. The 10 nm Ti top electrode with a 20 nm Pt capping layer are deposited by an e-beam evaporation process. For more details on the fabrication and the ALD process, the reader is referred to ref 88, as the VCM cells used for this study were fabricated with an analogous process.

https://doi.org/10.1021/acsaelm.1c00398
ACS Appl. Electron. Mater. 2021, 3, 3674−3692

AUTHOR INFORMATION

Corresponding Author

Stephan Menzel − *Peter Grünberg Institut (PGI-7), Forschungszentrum Juelich GmbH, 52425 Juelich, Germany;* orcid.org/0000-0002-4258-2673; Email: st.menzel@fz-juelich.de

Author

Carsten Funck − *Institut für Werkstoffe der Elektrotechnik 2, RWTH Aachen University, 52074 Aachen, Germany*

Complete contact information is available at: https://pubs.acs.org/10.1021/acsaelm.1c00398

Notes

The authors declare no competing financial interest.

ACKNOWLEDGMENTS

This work was supported in part by the Deutsche Forschungsgemeinschaft under Project SFB 917 and in part by the Federal Ministry of Education and Research (BMBF, Germany) in the Project Neuro-inspirierte Technologien der künstlichen Intelligenz (NEUROTEC) under grants 16ES1134 and 16ES1133K. It is based on the Jülich Aachen Research Alliance (JARA-FIT). The authors gratefully acknowledge the computing time granted for the project cjpgi70 by the JARA-HPC Vergabegremium on the supercomputer JURECA at the Forschungszentrum Jülich.[200] Prof. Rainer Waser is acknowledged for carefully reviewing the manuscript and for productive discussions. Alexander Hardtdegen is acknowledged for providing the resistive switching measurement of HfO_2 based VCM cells. Christoph Bäumer is acknowledged for the sample fabrication of the $SrTiO_3$ VCM cell and technical support. Susanne Hoffmann-Eifert and Regina Dittmann are acknowledged for fruitful discussions.

REFERENCES

(1) Waser, R.; Dittmann, R.; Staikov, G.; Szot, K. Redox-Based Resistive Switching Memories-Nanoionic Mechanisms, Prospects, and Challenges. *Adv. Mater.* **2009**, *21*, 2632−2663.

(2) Yang, J. J.; Inoue, I. H.; Mikolajick, T.; Hwang, C. S. Metal oxide memories based on thermochemical and valence change mechanisms. *MRS Bull.* **2012**, *37*, 131−137.

(3) Slesazeck, S.; Mikolajick, T. Nanoscale resistive switching memory devices: a review. *Nanotechnology* **2019**, *30*, 352003−23.

(4) Kim, K. M.; Jeong, D. S.; Hwang, C. S. Nanofilamentary resistive switching in binary oxide system a review on the present status and outlook. *Nanotechnology* **2011**, *22*, 254002.

(5) Waser, R.; Aono, M. Nanoionics-based resistive switching memories. *Nat. Mater.* **2007**, *6*, 833−840.

(6) Sebastian, A.; Le Gallo, M.; Khaddam-Aljameh, R.; Eleftheriou, E. Memory devices and applications for in-memory computing. *Nat. Nanotechnol.* **2020**, *15*, 529.

(7) Wang, Z.; Wu, H.; Burr, G. W.; Hwang, C. S.; Wang, K. L.; Xia, Q.; Yang, J. J. Resistive switching materials for information processing. *Nat. Rev. Mater.* **2020**, *5*, 173−195.

(8) Zhu, J.; Zhang, T.; Yang, Y.; Huang, R. A comprehensive review on emerging artificial neuromorphic devices. *Appl. Phys. Rev.* **2020**, *7*, 11312−107.

(9) Xia, Q.; Yang, J. J. Memristive crossbar arrays for brain-inspired computing. *Nat. Mater.* **2019**, *18*, 309−323.

(10) Hong, X.; Loy, D. J.; Dananjaya, P. A.; Tan, F.; Ng, C.; Lew, W. Oxide-based RRAM materials for neuromorphic computing. *J. Mater. Sci.* **2018**, *53*, 8720−8746.

(11) Ielmini, D.; Wong, H. P. In-memory computing with resistive switching devices. *Nature Electronics* **2018**, *1*, 333−343.

(12) Burr, G. W.; Shelby, R. M.; Sebastian, A.; Kim, S.; Kim, S.; Sidler, S.; Virwani, K.; Ishii, M.; Narayanan, P.; Fumarola, A.; Sanches, L. L.; Boybat, I.; Le Gallo, M.; Moon, K.; Woo, J.; Hwang, H.; Leblebici, Y. Neuromorphic computing using non-volatile memory. *Adv. Phys.-X* **2017**, *2*, 89−124.

(13) Hu, M.; Strachan, J. P.; Li, Z.; Merced Grafals, E.; Davila, N.; Graves, C.; Lam, S.; Ge, N.; Williams, R. S.; Yang, J. Dot-Product Engine for Neuromorphic Computing: Programming 1T1M Crossbar to Accelerate Matrix-Vector Multiplication. *53rd Design Automation Conference*, 2016.

(14) Gu, P.; Li, B.; Tang, T.; Yu, S.; Cao, Y.; Wang, Y.; Yang, H. Technological Exploration of RRAM Crossbar Array for Matrix-Vector Multiplication. *IEEE 20th Asia and South Pacific Design Automation Conference (ASP-DAC)* **2015**, 106−111.

(15) Le Gallo, M.; Sebastian, A.; Mathis, R.; Manica, M.; Giefers, H.; Tuma, T.; Bekas, C.; Curioni, A.; Eleftheriou, E. Mixed-precision in-memory computing. *Nature Electronics* **2018**, *1*, 246−253.

(16) Le Gallo, M.; Sebastian, A.; Cherubini, G.; Giefers, H.; Eleftheriou, E. Compressed Sensing With Approximate Message Passing Using In-Memory Computing. *IEEE Trans. Electron Devices* **2018**, *65*, 4304−4312.

(17) Li, C.; Wang, Z.; Rao, M.; Belkin, D.; Song, W.; Jiang, H.; Yan, P.; Li, Y.; Lin, P.; Hu, M.; Ge, N.; Strachan, J. P.; Barnell, M.; Wu, Q.; Williams, R. S.; Yang, J. J.; Xia, Q. Long short-term memory networks in memristor crossbar arrays. *Nature Machine Intelligence* **2019**, *1*, 49−57.

(18) Wang, Z.; Li, C.; Lin, P.; Rao, M.; Nie, Y.; Song, W.; Qiu, Q.; Li, Y.; Yan, P.; Strachan, J. P.; Ge, N.; McDonald, N.; Wu, Q.; Hu, M.; Wu, H.; Williams, R. S.; Xia, Q.; Yang, J. J. In situ training of feed-forward and recurrent convolutional memristor networks. *Nat. Mach. Intell.* **2019**, *1*, 434−442.

(19) Wang, Z.; Li, C.; Song, W.; Rao, M.; Belkin, D.; Li, Y.; Yan, P.; Jiang, H.; Lin, P.; Hu, M.; Strachan, J. P.; Ge, N.; Barnell, M.; Wu, Q.; Barto, A. G.; Qiu, Q.; Williams, R. S.; Xia, Q.; Yang, J. J. Reinforcement learning with analogue memristor arrays. *Nat. Electron.* **2019**, *2*, 115−124.

(20) Brivio, S.; Ly, D. R. B.; Vianello, E.; Spiga, S. Non-linear Memristive Synaptic Dynamics for Efficient Unsupervised Learning in Spiking Neural Networks. *Front. Neurosci.* **2021**, *15*, 580909.

(21) Naous, R.; Siemon, A.; Schulten, M.; Alahmadi, H.; Kindsmüller, A.; Lübben, M.; Heittmann, A.; Waser, R.; Salama, K. N.; Menzel, S. Theory and experimental verification of configurable computing with stochastic memristors. *Sci. Rep.* **2021**, *11*, 4218.

(22) Hoffer, B.; Rana, V.; Menzel, S.; Waser, R.; Kvatinsky, S. Experimental Demonstration of Memristor-Aided Logic (MAGIC) Using Valence Change Memory (VCM). *IEEE Trans. Electron Devices* **2020**, *67*, 3115−3122.

(23) Giannopoulos, I.; Singh, A.; Le Gallo, M.; Jonnalagadda, V. P.; Hamdioui, S.; Sebastian, A. In-Memory Database Query. *Advanced Intelligent Systems* **2020**, *2*, 2000141.

(24) Kim, Y. S.; Son, M. W.; Song, H.; Park, J.; An, J.; Jeon, J. B.; Kim, G. Y.; Son, S.; Kim, K. M. Stateful In-Memory Logic System and Its Practical Implementation in a TaO_x-Based Bipolar-Type Memristive Crossbar Array. *Adv. Intell. Syst.* **2020**, *2*, 1900156.

(25) Wang, X.; Zidan, M. A.; Lu, W. D. A Crossbar-Based In-Memory Computing Architecture. *IEEE Transactions on Circuits and Systems I: Regular Papers* **2020**, *67*, 4224−4232.

(26) Xu, N.; Park, T. G.; Kim, H. J.; Shao, X.; Yoon, K. J.; Park, T. H.; Fang, L.; Kim, K. M.; Hwang, C. S. A Stateful Logic Family Based on a New Logic Primitive Circuit Composed of Two Antiparallel Bipolar Memristors. *Advanced Intelligent Systems* **2020**, *2*, 1900082.

(27) Yoon, K. J.; Han, J.; Bae, W. A Novel Stateful Logic Device and Circuit for In-Memory Parity Programming in Crossbar Memory. *Advanced Electronic Materials* **2020**, *6*, 2000672.

(28) Zanotti, T.; Puglisi, F. M.; Pavan, P. Smart Logic-in-Memory Architecture for Low-Power Non-Von Neumann Computing. *IEEE J. Electron Devices Soc.* **2020**, *8*, 757−764.

(29) Papandroulidakis, G.; Serb, A.; Khiat, A.; Merrett, G. V.; Prodromakis, T. Practical Implementation of Memristor-Based

Threshold Logic Gates. *IEEE Transactions on Circuits and Systems I: Regul* **2019**, *66*, 3041−3051.
(30) Siemon, A.; Drabinski, R.; Schultis, M. J.; Hu, X.; Linn, E.; Heittmann, A.; Waser, R.; Querlioz, D.; Menzel, S.; Friedman, J. S. Stateful Three-Input Logic with Memristive Switches. *Sci. Rep.* **2019**, *9*, 14618−13.
(31) Siemon, A.; Menzel, S.; Bhattacharjee, D.; Waser, R.; Chattopadhyay, A.; Linn, E. Sklansky tree adder realization in 1S1R resistive switching memory architecture. *Eur. Phys. J.: Spec. Top.* **2019**, *228*, 2269−2285.
(32) Bhattacharjee, D.; Kim, W.; Chattopadhyay, A.; Waser, R.; Rana, V. Multi-valued and Fuzzy Logic Realization using TaOx Memristive Devices. *Sci. Rep.* **2018**, *8*, 1−10.
(33) Jang, B. C.; Nam, Y.; Koo, B. J.; Choi, J.; Im, S. G.; Park, S.-H. K.; Choi, S.-Y. Memristive Logic-in-Memory Integrated Circuits for Energy-Efficient Flexible Electronics. *Adv. Funct. Mater.* **2018**, *28*, 1704725.
(34) Xu, N.; Yoon, K. J.; Kim, K. M.; Fang, L.; Hwang, C. S. Fully Functional Logic-In-Memory Operations Based on a Reconfigurable Finite-State Machine Using a Single Memristor. *Advanced Electronic Materials* **2018**, *4*, 1800189.
(35) Han, R.; Huang, P.; Zhao, Y.; Chen, Z.; Liu, L.; Liu, X.; Kang, J. Demonstration of Logic Operations in High-Performance RRAM Crossbar Array Fabricated by Atomic Layer Deposition Technique. *Nanoscale Res. Lett.* **2017**, *12*, 37−6.
(36) Papandroulidakis, G.; Vourkas, I.; Abusleme, A.; Sirakoulis, G. Ch.; Rubio, A. Crossbar-Based Memristive Logic-in-Memory Architecture. *IEEE Trans. Nanotechnol.* **2017**, *16*, 491−501.
(37) Wang, Z. R.; Su, Y. T.; Li, Y.; Zhou, Y. X.; Chu, T. J.; Chang, K. C.; Chang, T. C.; Tsai, T. M.; Sze, S. M.; Miao, X. S. Functionally Complete Boolean Logic in 1T1R Resistive Random Access Memory. *IEEE Electron Device Lett.* **2017**, *38*, 179−182.
(38) Adam, G. C.; Hoskins, B. D.; Prezioso, M.; Strukov, D. B. Optimized stateful material implication logic for threedimensional data manipulation. *Nano Res.* **2016**, *9*, 3914.
(39) Breuer, T.; Nielen, L.; Roesgen, B.; Waser, R.; Rana, V.; Linn, E. Realization of Minimum and Maximum Gate Function in Ta_2O_5-based Memristive Devices. *Sci. Rep.* **2016**, *6*, 23967−9.
(40) Gaillardon, P.-E.; Amaru, L.; Siemon, A.; Linn, E.; Waser, R.; Chattopadhyay, A.; De Micheli, G. The Programmable Logic-in-Memory (PLiM) Computer. In *2016 Design, Automation & Test in Europe Conference & Exhibition (DATE)*, Dresden, Germany, March 14−18, 2016; pp 1−6.
(41) Kim, W.; Chattopadhyay, A.; Siemon, A.; Linn, E.; Waser, R.; Rana, V. Multistate Memristive Tantalum Oxide Devices for Ternary Arithmetic. *Sci. Rep.* **2016**, *6*, 36652.
(42) Talati, N.; Gupta, S.; Mane, P.; Kvatinsky, S. Logic Design Within Memristive Memories Using Memristor-Aided loGIC (MAGIC). *IEEE Trans. Nanotechnol.* **2016**, *15*, 635−650.
(43) Vourkas, I.; Sirakoulis, G. Ch. Emerging Memristor-Based Logic Circuit Design Approaches: A Review. *IEEE Circuits and Systems Magazine* **2016**, *16*, 15−30.
(44) Breuer, T.; Siemon, A.; Linn, E.; Menzel, S.; Waser, R.; Rana, V. A HfO2-Based Complementary Switching Crossbar Adder. *Adv. Electron. Mater.* **2015**, *1*, 1500138.
(45) Siemon, A.; Menzel, S.; Waser, R.; Linn, E. A Complementary Resistive Switch-based Crossbar Array Adder. *IEEE J. Emerging Sel. Top. Circuits Syst.* **2015**, *5*, 64−74.
(46) Siemon, A.; Breuer, T.; Aslam, N.; Ferch, S.; Kim, W.; van den Hurk, J.; Rana, V.; Hoffmann-Eifert, S.; Waser, R.; Menzel, S.; Linn, E. Realization of Boolean Logic Functionality using Redox-based Memristive Devices. *Adv. Funct. Mater.* **2015**, *25*, 6414−6423.
(47) Kvatinsky, S.; Belousov, D.; Liman, S.; Satat, G.; Wald, N.; Friedman, E. G.; Kolodny, A.; Weiser, U. C. MAGIC-Memristor-Aided Logic. *IEEE Trans. Circuits Syst. II-Express Briefs* **2014**, *61*, 895−899.
(48) Rosezin, R.; Linn, E.; Kügeler, C.; Bruchhaus, R.; Waser, R. Crossbar Logic Using Bipolar and Complementary Resistive Switches. *IEEE Electron Device Lett.* **2011**, *32*, 710−712.
(49) Sousa, V. Chalcogenide materials and their application to Non-Volatile Memories. *Microelectron. Eng.* **2011**, *88*, 807−813.
(50) Parkin, S. S. P.; Kaiser, C.; Panchula, A.; Rice, P. M.; Hughes, B.; Samant, M.; Yang, S.-H. Giant tunnelling magnetoresistance at room temperature with MgO (100) tunnel barriers. *Nat. Mater.* **2004**, *3*, 862−7.
(51) Lee, H. S.; Han, W.; Chung, H. Y.; Rozenberg, M.; Kim, K.; Lee, Z.; Yeom, G. Y.; Park, H. H. Ferroelectric Tunnel Junction for Dense Cross-Point Arrays. *ACS Appl. Mater. Interfaces* **2015**, *7*, 22348−22354.
(52) Borghetti, J.; Snider, G. S.; Kuekes, P. J.; Yang, J. J.; Stewart, D. R.; Williams, R. S. 'Memristive' switches enable 'stateful' logic operations via material implication. *Nature* **2010**, *464*, 873−876.
(53) Bengel, C.; Cüppers, F.; Payvand, M.; Dittmann, R.; Waser, R.; Hoffmann-Eifert, S.; Menzel, S. Utilizing the Switching Stochasticity of HfO2/TiOx-Based ReRAM Devices and the Concept of Multiple Devices for the Classification of Overlapping and Noisy Patterns. *Front. Neurosci.* **2021**, *15*, 621.
(54) Boybat, I.; Le Gallo, M.; Nandakumar, S. R.; Moraitis, T.; Parnell, T.; Tuma, T.; Rajendran, B.; Leblebici, Y.; Sebastian, A.; Eleftheriou, E. Neuromorphic computing with multi-memristive synapses. *Nat. Commun.* **2018**, *9*, 2514.
(55) Kim, W.; Menzel, S.; Wouters, D. J.; Guo, Y.; Robertson, J.; Rösgen, B.; Waser, R.; Rana, V. Impact of oxygen exchange reaction at the ohmic interface in Ta_2O_5-based ReRAM devices. *Nanoscale* **2016**, *8*, 17774−17781.
(56) Maier, J. *Physical Chemistry of Ionic Materials*; Wiley, 2004.
(57) Kroeger, F. A.; Vink, H. J. Relations between the Concentrations of Imperfections in Crystalline Solids. *Solid State Phys.* **1956**, *3*, 307−435.
(58) Yang, J. J.; Miao, F.; Pickett, M. D.; Ohlberg, D. A. A.; Stewart, D. R.; Lau, C. N.; Williams, R. S. The mechanism of electroforming of metal oxide memristive switches. *Nanotechnology* **2009**, *20*, 215201.
(59) Marchewka, A.; Waser, R.; Menzel, S. Physical Modeling of the Electroforming Process in Resistive-Switching Devices (talk). In *2017 International Conference on Simulation of Semiconductor Processes and Devices (SISPAD)*, September 7−9, Kamakura, Japan, 2017.
(60) Abbaspour, E.; Menzel, S.; Hardtdegen, A.; Hoffmann-Eifert, S.; Jungemann, C. KMC Simulation of the Electroforming, Set and Reset Processes in Redox-based Resistive Switching Devices. *IEEE Trans. Nanotechnol.* **2018**, *17*, 1181−1188.
(61) Larentis, S.; Nardi, F.; Balatti, S.; Gilmer, D. C.; Ielmini, D. Resistive Switching by Voltage-Driven Ion Migration in Bipolar RRAM-Part II: Modeling. *IEEE Trans. Electron Devices* **2012**, *59*, 2468−2475.
(62) Larentis, S.; Nardi, F.; Balatti, S.; Ielmini, D.; Gilmer, D. C. Bipolar-switching model of RRAM by field-and temperature-activated ion migration. *2012 4th IEEE International Memory Workshop (IMW)* **2012**, 4.
(63) Szot, K.; Speier, W.; Bihlmayer, G.; Waser, R. Switching the electrical resistance of individual dislocations in single-crystalline $SrTiO_3$. *Nat. Mater.* **2006**, *5*, 312−320.
(64) Strukov, D. B.; Borghetti, J. L.; Williams, R. S. Coupled Ionic and Electronic Transport Model of Thin-Film Semiconductor Memristive Behavior. *Small* **2009**, *5*, 1058−1063.
(65) Yang, J. J.; Pickett, M. D.; Li, X.; Ohlberg, D. A. A.; Stewart, D. R.; Williams, R. S. Memristive switching mechanism for metal/oxide/metal nanodevices. *Nat. Nanotechnol.* **2008**, *3*, 429−433.
(66) Borghetti, J.; Strukov, D. B.; Pickett, M. D.; Yang, J. J.; Stewart, D. R.; Williams, R. S. Electrical transport and thermometry of electroformed titanium dioxide memristive switches. *J. Appl. Phys.* **2009**, *106*, 124504−5.
(67) Cooper, D.; Baeumer, C.; Bernier, N.; Marchewka, A.; La Torre, C.; Dunin-Borkowski, R. E.; Menzel, S.; Waser, R.; Dittmann, R. Anomalous Resistance Hysteresis in Oxide ReRAM: Oxygen Evolution and Reincorporation Revealed by in situ TEM. *Adv. Mater.* **2017**, *29*, 1700212.
(68) Zhang, H.; Yoo, S.; Menzel, S.; Funck, C.; Cueppers, F.; Wouters, D. J.; Hwang, C. S.; Waser, R.; Hoffmann-Eifert, S.

https://doi.org/10.1021/acsaelm.1c00398
ACS Appl. Electron. Mater. 2021, 3, 3674−3692

Understanding the Coexistence of Two Bipolar Resistive Switching Modes with Opposite Polarity in Pt/TiO_2/Ti/Pt Nanosized ReRAM Devices. *ACS Appl. Mater. Interfaces* **2018**, *10*, 29766−29778.
(69) Lee, M.-J.; Lee, C. B.; Lee, D.; Lee, S. R.; Chang, M.; Hur, J. H.; Kim, Y.-B.; Kim, C.-J.; Seo, D. H.; Seo, S.; Chung, U.-I.; Yoo, I.-K.; Kim, K. A fast, high-endurance and scalable non-volatile memory device made from asymmetric Ta_2O_{5-x}/TaO_{2-x} bilayer structures. *Nat. Mater.* **2011**, *10*, 625−630.
(70) Govoreanu, B.; Ajaykumar, A.; Lipowicz, H.; Chen, Y.; Liu, J.; Degraeve, R.; Zhang, L.; Clima, S.; Goux, L.; Radu, I.; Fantini, A.; Raghavan, N.; Kar, G.; Kim, W.; Redolfi, A.; Wouters, D.; Altimime, L.; Jurczak, M. Performance and Reliability of Ultra-Thin HfO2-based RRAM (UTO-RRAM). *2013 5th IEEE International Memory Workshop (IMW)* **2013**, 48−51.
(71) Wiefels, S.; von Witzleben, M.; Hüttemann, M.; Böttger, U.; Waser, R.; Menzel, S. Impact of the Ohmic Electrode on the Endurance of Oxide Based Resistive Switching Memory. *IEEE Trans. Electron Devices* **2021**, *68*, 1024−1030.
(72) Mohan, C.; Camunas-Mesa, L. A.; de la Rosa, J. M.; Vianello, E.; Serrano-Gotarredona, T.; Linares-Barranco, B. Neuromorphic Low-Power Inference on Memristive Crossbars With On-Chip Offset Calibration. *IEEE Access* **2021**, *9*, 38043−38061.
(73) Yang, F.; Liu, F.; Ji, F.; Lin, Y.; Tang, M. Origin of resistive-switching behaviors of chemical solution deposition-derived BiFeO3 thin-film memristors. *Mater. Adv.* **2020**, *1*, 2117−2123.
(74) Sassine, G.; La Barbera, S.; Najjari, N.; Minvielle, M.; Dubourdieu, C.; Alibart, F. Interfacial versus filamentary resistive switching in TiO2 and HfO2 devices. *J. Vac. Sci. Technol., B: Nanotechnol. Microelectron.: Mater., Process., Meas., Phenom.* **2016**, *34*, 12202.
(75) Zhang, Q.; Rana, A.; Liu, X.; Valanoor, N. Electrode Dependence of Local Electrical Properties of Chemical-Solution-Deposition-Derived BiFeO3 Thin Films. *ACS Applied Electronic Materials* **2019**, *1*, 154−162.
(76) Baeumer, C.; Funck, C.; Locatelli, A.; Mentes, T. O.; Genuzio, F.; Heisig, T.; Hensling, F.; Raab, N.; Schneider, C. M.; Menzel, S.; Waser, R.; Dittmann, R. In-Gap States and Band-Like Transport in Memristive Devices. *Nano Lett.* **2019**, *19*, 54−60.
(77) Xiong, Y. Q.; Zhou, W. P.; Li, Q.; Cao, Q. Q.; Tang, T.; Wang, D. H.; Du, Y. W. Electric field modification of magnetism in Au/La2/3Ba1/3MnO3/Pt device. *Sci. Rep.* **2015**, *5*, 12766−7.
(78) Chakrabarti, S.; Samanta, S.; Maikap, S.; Rahaman, S. Z.; Cheng, H. M. Temperature-Dependent Non-linear Resistive Switching Characteristics and Mechanism Using a New W/WO3/WOx/W Structure. *Nanoscale Res. Lett.* **2016**, *11*, 389−8.
(79) Liu, X.; Nandi, S. K.; Venkatachalam, D. K.; Li, S.; Belay, K.; Elliman, R. G. Finite Element Modeling of Resistive Switching in Nb2O5-based Memory Device. In *Conference on Optoelectronic and Microelectronic Materials and Devices (COMMAD)*, Univ Western Australia, Perth, Australia, 2014; pp 280−282.
(80) Park, T. H.; Song, S. J.; Kim, H. J.; Kim, S. G.; Chung, S.; Kim, B. Y.; Lee, K. J.; Kim, K. M.; Choi, B. J.; Hwang, C. S. Thickness effect of ultra-thin Ta_2O_5 resistance switching layer in 28 nm-diameter memory cell. *Sci. Rep* **2015**, *5*, 15965−9.
(81) Kim, T.; Son, H.; Kim, I.; Kim, J.; Lee, S.; Park, J. K.; Kwak, J. Y.; Park, J.; Jeong, Y. Reversible switching mode change in Ta2O5-based resistive switching memory (ReRAM). *Sci. Rep.* **2020**, *10*, 11247.
(82) Lin, C.; Lin, T. Superior unipolar resistive switching in stacked ZrOx/ZrO2/ZrOx structure. *AIP Adv.* **2016**, *6*, 035103.
(83) Huang, R.; Yan, X.; Morgan, K. A.; Charlton, M. D. B.; de Groot, C. H. Selection by current compliance of negative and positive bipolar resistive switching behaviour in ZrO2-x/ZrO2 bilayer memory. *J. Phys. D: Appl. Phys.* **2017**, *50*, 175101−9.
(84) Khan, M. U.; Hassan, G.; Bae, J. Non-volatile resistive switching based on zirconium dioxide: poly (4-vinylphenol) nano-composite. *Appl. Phys. A: Mater. Sci. Process.* **2019**, *125*, 378−11.
(85) Zeng, B.; Xu, D.; Tang, M.; Xiao, Y.; Zhou, Y.; Xiong, R.; Li, Z.; Zhou, Y. Improvement of resistive switching performances via an amorphous ZrO2 layer formation in TiO2-based forming-free resistive random access memory. *J. Appl. Phys.* **2014**, *116*, 124514−4.
(86) Kumar, S.; Wang, Z.; Huang, X.; Kumari, N.; Davila, N.; Strachan, J. P.; Vine, D.; Kilcoyne, A. L.; Nishi, Y.; Williams, R. S. Oxygen migration during resistance switching and failure of hafnium oxide memristors. *Appl. Phys. Lett.* **2017**, *110*, 103503.
(87) Cueppers, F.; Menzel, S.; Bengel, C.; Hardtdegen, A.; von Witzleben, M.; Boettger, U.; Waser, R.; Hoffmann-Eifert, S. Exploiting the switching dynamics of HfO2-based ReRAM devices for reliable analog memristive behavior. *APL Mater.* **2019**, *7*, 91105−9.
(88) Hardtdegen, A.; La Torre, C.; Cüppers, F.; Menzel, S.; Waser, R.; Hoffmann-Eifert, S. Improved Switching Stability and the Effect of an Internal Series Resistor in HfO_2/TiO_x Bilayer ReRAM Cells. *IEEE Trans. Electron Devices* **2018**, *65*, 3229−3236.
(89) Guo, T.; Tan, T.; Liu, Z. The effect of Cu doping concentration on resistive switching of HfO2 film. *Appl. Surf. Sci.* **2015**, *351*, 704−708.
(90) Qian, M.; Fina, I.; Sanchez, F.; Fontcuberta, J. Asymmetric Resistive Switching Dynamics in BaTiO3 Tunnel Junctions. *Adv. Electron. Mater.* **2019**, *5*, 1800407−8.
(91) Yang, G.; Jia, C. H.; Chen, Y. H.; Chen, X.; Zhang, W. F. Negative differential resistance and resistance switching behaviors in BaTiO3 thin films. *J. Appl. Phys.* **2014**, *115*, 204515.
(92) Lv, F.; Gao, C.; Zhang, P.; Dong, C.; Zhang, C.; Xue, D. Bipolar resistive switching behavior of CaTiO3 films grown by hydrothermal epitaxy. *RSC Adv.* **2015**, *5*, 40714−40718.
(93) Lin, Z. H.; Wang, Y. H. Observation of indium ion migration-induced resistive switching in Al/Mg0.5Ca0.5TiO3/ITO. *Appl. Phys. Lett.* **2016**, *109*, 53507−4.
(94) Hsieh, W. K.; Lam, K. T.; Chang, S. J. Asymmetric resistive switching characteristics of In2O3:SiO2 cosputtered thin film memories. *J. Vac. Sci. Technol., B: Nanotechnol. Microelectron.: Mater., Process., Meas., Phenom.* **2014**, *32*, 20603.
(95) Nieh, C. H.; Lu, M. L.; Weng, T. M.; Chen, Y. F. Resistive memory of single SnO2 nanowire based switchable diodes. *Appl. Phys. Lett.* **2014**, *104*, 213501−4.
(96) Kim, W.; Menzel, S.; Wouters, D. J.; Waser, R.; Rana, V. 3-Bit Multi Level Switching by Deep Reset Phenomenon in Pt/W/TaO_x/Pt-ReRAM Devices. *IEEE Electron Device Lett.* **2016**, *37*, 564−567.
(97) Mondal, S.; Her, J. L.; Koyama, K.; Pan, T. M. Resistive switching behavior in Lu2O3 thin film for advanced flexible memory applications. *Nanoscale Res. Lett.* **2014**, *9*, 3−8.
(98) Shen, W.; Dittmann, R.; Waser, R. Reversible alternation between bipolar and unipolar resistive switching in polycrystalline barium strontium titanate thin films. *J. Appl. Phys.* **2010**, *107*, 94506−4.
(99) Gao, S.; Liu, G.; Chen, Q.; Xue, W.; Yang, H.; Shang, J.; Chen, B.; Zeng, F.; Song, C.; Pan, F.; Li, R. W. Improving Unipolar Resistive Switching Uniformity with Cone Shaped Conducting Filaments and Its Logic-In-Memory Application. *ACS Appl. Mater. Interfaces* **2018**, *10*, 6453−6462.
(100) Funck, C.; Bäumer, C.; Wiefels, S.; Hennen, T.; Waser, R.; Hoffmann-Eifert, S.; Dittmann, R.; Menzel, S. Comprehensive model for the electronic transport in Pt/$SrTiO_3$ analog memristive devices. *Phys. Rev. B: Condens. Matter Mater. Phys.* **2020**, *102*, 035307.
(101) Linderälv, C.; Lindman, A.; Erhart, P. A Unifying Perspective on Oxygen Vacancies in Wide Band Gap Oxides. *J. Phys. Chem. Lett.* **2018**, *9*, 222−228.
(102) Gavartin, J. L.; Muñoz Ramo, D.; Shluger, A. L.; Bersuker, G.; Lee, B. H. Negative oxygen vacancies in HfO2 as charge traps in high-k stacks. *Appl. Phys. Lett.* **2006**, *89*, 082908.
(103) Xiong, K.; Robertson, J.; Gibson, M. C.; Clark, S. J. Defect energy levels in HfO2 high-dielectric-constant gate oxide. *Appl. Phys. Lett.* **2005**, *87*, 183505.
(104) Xiong, K.; Robertson, J. Point defects in HfO2 high K gate oxide. *Microelectron. Eng.* **2005**, *80*, 408−411.
(105) Broqvist, P.; Pasquarello, A. Oxygen vacancy in monoclinic HfO2: A consistent interpretation of trap assisted conduction, direct

https://doi.org/10.1021/acsaelm.1c00398
ACS Appl. Electron. Mater. 2021, 3, 3674−3692

electron injection, and optical absorption experiments. *Appl. Phys. Lett.* **2006**, *89*, 262904−3.
(106) Cimino, S.; Padovani, A.; Larcher, L.; Afanas'ev, V. V.; Hwang, H. J.; Lee, Y. G.; Jurczac, M.; Wouters, D.; Lee, B. H.; Hwang, H.; Pantisano, L. A study of the leakage current in TiN/HfO2/TiN capacitors. *Microelectron. Eng.* **2012**, *95*, 71−73.
(107) Bersuker, G.; Yum, J.; Vandelli, L.; Padovani, A.; Larcher, L.; Iglesias, V.; Porti, M.; Nafria, M.; McKenna, K.; Shluger, A.; Kirsch, P.; Jammy, R. Grain boundary-driven leakage path formation in HfO2 dielectrics. *Solid-State Electron.* **2011**, *65*−*66*, 146−150.
(108) Pirrotta, O.; Larcher, L.; Lanza, M.; Padovani, A.; Porti, M.; Nafria, M.; Bersuker, G. Leakage current through the poly-crystalline HfO2: Trap densities at grains and grain boundaries. *J. Appl. Phys.* **2013**, *114*, 134503−5.
(109) Yan, X.; Zhou, Z.; Ding, B.; Zhao, J.; Zhang, Y. Superior resistive switching memory and biological synapse properties based on a simple TiN/SiO2/p-Si tunneling junction structure. *J. Mater. Chem. C* **2017**, *5*, 2259−2267.
(110) Gismatulin, A.; Gritsenko, V.; Perevalov, T.; Kuzmichev, D.; Chernikova, A.; Markeev, A. Charge Transport Mechanism in Atomic Layer Deposited Oxygen-Deficient TaOx Films. *Phys. Status Solidi B* **2021**, *258*, 2000432−6.
(111) Miron, D.; Cohen-Azarzar, D.; Segev, N.; Baskin, M.; Palumbo, F.; Yalon, E.; Kornblum, L. Band structure and electronic transport across Ta_2O_5/Nb:$SrTiO_3$ interfaces. *J. Appl. Phys.* **2020**, *128*, 045306.
(112) Ryu, H.; Kim, S. Gradually Tunable Conductance in TiO2/Al2O3 Bilayer Resistors for Synaptic Device. *Metals* **2021**, *11*, 440.
(113) Beilliard, Y.; Paquette, F.; Brousseau, F.; Ecoffey, S.; Alibart, F.; Drouin, D. Investigation of resistive switching and transport mechanisms of Al2O3/TiO2-x memristors under cryogenic conditions (1.5 K). *AIP Adv.* **2020**, *10*, 025305.
(114) Chen, X. G.; Fu, J. B.; Liu, S. Q.; Yang, Y. B.; Wang, C. S.; Du, H. L.; Xiong, G. C.; Lian, G. J.; Yang, J. B. Trap-assisted tunneling resistance switching effect in CeO2/La-0.7(Sr0.1Ca0.9)(0.3)MnO3 heterostructure. *Appl. Phys. Lett.* **2012**, *101*, 153509−4.
(115) Yu, S.; Guan, X.; Wong, H. P. Conduction mechanism of TiN/HfOx/Pt resistive switching memory: A trap-assisted-tunneling model. *Appl. Phys. Lett.* **2011**, *99*, 063507−063507.
(116) Fang, R.; Chen, W.; Gao, L.; Yu, W.; Yu, S. Low-Temperature Characteristics of HfOx-Based Resistive Random Access Memory. *IEEE Electron Device Lett.* **2015**, *36*, 567−569.
(117) Wong, H.-S. P.; Lee, H.-Y.; Yu, S.; Chen, Y.-S.; Wu, Y.; Chen, P.-S.; Lee, B.; Chen, F. T.; Tsai, M.-J. Metal-Oxide RRAM. *Proc. IEEE* **2012**, *100*, 1951−1970.
(118) Yu, S.; Jeyasingh, R.; Wu, Y.; Wong, H. Understanding the Conduction and Switching Mechanism of Metal Oxide RRAM through Low Frequency Noise and AC Conductance Measurement and Analysis. In *IEEE International Electron Devices Meeting (IEDM)*, Washington, DC, 2011.
(119) Yu, S.; Ximeng Guan; Wong, H.-S. P. On the Stochastic Nature of Resistive Switching in Metal Oxide RRAM: Physical Modeling, Monte Carlo Simulation, and Experimental Characterization. *2011 IEEE International Electron Devices Meeting (IEDM)* **2011**, 17.3.1−17.3.4.
(120) Yu, S.; Jeyasingh, R.; Wu, Y.; Wong, H. Characterization of low-frequency noise in the resistive switching of transition metal oxide HfO2. *Phys. Rev. B: Condens. Matter Mater. Phys.* **2012**, *85*, 45324−5.
(121) Dirkmann, S.; Mussenbrock, T. Resistive switching in memristive electrochemical metallization devices. *AIP Adv.* **2017**, *7*, 065006.
(122) Dirkmann, S.; Kaiser, J.; Wenger, C.; Mussenbrock, T. Filament Growth and Resistive Switching in Hafnium Oxide Memristive Devices. *ACS Appl. Mater. Interfaces* **2018**, *10*, 14857−14868.
(123) Bersuker, G.; Gilmer, D. C.; Veksler, D.; Kirsch, P.; Vandelli, L.; Padovani, A.; Larcher, L.; McKenna, K.; Shluger, A.; Iglesias, V.; Porti, M.; Nafria, M. Metal oxide resistive memory switching mechanism based on conductive filament properties. *J. Appl. Phys.* **2011**, *110*, 124518.
(124) Yu, S.; Wu, Y.; Wong, H. Investigating the switching dynamics and multilevel capability of bipolar metal oxide resistive switching memory. *Appl. Phys. Lett.* **2011**, *98*, 103514−3.
(125) Houng, M.; Wang, Y.; Chang, W. Current transport mechanism in trapped oxides: A generalized trap-assisted tunneling model. *J. Appl. Phys.* **1999**, *86*, 1488−1491.
(126) Chuang, K.-C.; Chu, C.-Y.; Zhang, H.-X.; Luo, J.-D.; Li, W.-S.; Li, Y.-S.; Cheng, H.-C. Impact of the Stacking Order of HfOX and AlOX Dielectric Films on RRAM Switching Mechanisms to Behave Digital Resistive Switching and Synaptic Characteristics. *IEEE J. Electron Devices Soc.* **2019**, *7*, 589−595.
(127) Kim, S.; Park, B. G. Nonlinear and multilevel resistive switching memory in Ni/Si3N4/Al2O3/TiN structures. *Appl. Phys. Lett.* **2016**, *108*, 212103−5.
(128) Tamanna, N.; Misha, S. H.; Prakash, A.; Lee, D.; Woo, J.; Cha, E.; Attarimashalkoubeh, B.; Song, J.; Lee, S.; Moon, K.; Hwang, H. Non-Linear I-V Characteristics of TiOy Film by Optimizing Thickness and Trap Density for Selector-Less ReRAM. *ECS Solid State Lett.* **2014**, *3*, P117−P119.
(129) Linn, E.; Rosezin, R.; Kügeler, C.; Waser, R. Complementary Resistive Switches for Passive Nanocrossbar Memories. *Nat. Mater.* **2010**, *9*, 403−406.
(130) Marchewka, A.; Waser, R.; Menzel, S. Physical Simulation of Dynamic Resistive Switching in Metal Oxides Using a Schottky Contact Barrier Model. In *2015 International Conference On Simulation of Semiconductor Processes and Devices (SISPAD)*, September 9−11, Washington, D.C, USA, 2015; pp 297−300.
(131) Nardi, F.; Balatti, S.; Larentis, S.; Gilmer, D. C.; Ielmini, D. Complementary Switching in Oxide-Based Bipolar Resistive-Switching Random Memory. *IEEE Trans. Electron Devices* **2013**, *60*, 70−77.
(132) Egorov, K. V.; Kirtaev, R. V.; Lebedinskii, Y. Y.; Markeev, A. M.; Matveyev, Y. A.; Orlov, O. M.; Zablotskiy, A. V.; Zenkevich, A. V. Complementary and bipolar regimes of resistive switching in TiN/HfO2/TiN stacks grown by atomic-layer deposition. *Phys. Status Solidi A* **2015**, *212*, 809−816.
(133) Matveyev, Yu; Egorov, K.; Markeev, A.; Zenkevich, A. Resistive switching and synaptic properties of fully atomic layer deposition grown TiN/HfO2/TiN devices. *J. Appl. Phys.* **2015**, *117*, 44901−7.
(134) Yalon, E.; Gavrilov, A.; Cohen, S.; Mistele, D.; Meyler, B.; Salzman, J.; Ritter, D. Resistive Switching in HfO2 Probed by a Metal-Insulator-Semiconductor Bipolar Transistor. *IEEE Electron Device Lett.* **2012**, *33*, 11−13.
(135) Kuzmichev, D. S.; Chernikova, A. G.; Kozodaev, M. G.; Markeev, A. M. Resistance Switching Peculiarities in Nonfilamentary Self-Rectified TiN/Ta2O5/Ta and TiN/HfO2/Ta2O5/Ta Stacks. *Phys. Status Solidi A* **2020**, *217*, 1900952−8.
(136) Zhu, Y. B.; Zheng, K.; Wu, X.; Ang, L. K. Enhanced stability of filament-type resistive switching by interface engineering. *Sci. Rep* **2017**, *7*, 43664−7.
(137) Zhi, Y. S.; Li, P. G.; Wang, P. C.; Guo, D. Y.; An, Y. H.; Wu, Z. P.; Chu, X. L.; Shen, J. Q.; Tang, W. H.; Li, C. R. Reversible transition between bipolar and unipolar resistive switching in Cu2O/Ga2O3 binary oxide stacked layer. *AIP Adv.* **2016**, *6*, 15215−8.
(138) Petrov, A. A.; Andreeva, N. V.; Ivanov, A. S. Mechanism of electron transport and bipolar resistive switching in lead oxide thin films. *AIP Adv.* **2018**, *8*, 105015−7.
(139) Zhang, K.; Sun, K.; Wang, F.; Han, Y.; Jiang, Z.; Zhao, J.; Wang, B.; Zhang, H.; Jian, X.; Wong, H. S. P. Ultra-Low Power Ni/HfO2/TiOx/TiN Resistive Random Access Memory With Sub-30-nA Reset Current. *IEEE Electron Device Lett.* **2015**, *36*, 1018−1020.
(140) Liu, C. F.; Tang, X. G.; Wang, L. Q.; Tang, H.; Jiang, Y. P.; Liu, Q. X.; Li, W. H.; Tang, Z. H. Resistive Switching Characteristics of HfO2 Thin Films on Mica Substrates Prepared by Sol-Gel Process. *Nanomaterials* **2019**, *9*, 1124−11.

https://doi.org/10.1021/acsaelm.1c00398
ACS Appl. Electron. Mater. 2021, 3, 3674−3692

(141) Maikap, S.; Jana, D.; Dutta, M.; Prakash, A. Self-compliance RRAM characteristics using a novel W/TaOx/TiN structure. *Nanoscale Res. Lett.* **2014**, *9*, 292−6.
(142) Ismail, M.; Khan, S. A.; Rahmani, M. K.; Choi, J.; Batool, Z.; Rana, A. M.; Kim, S. Oxygen annealing effect on resistive switching characteristics of multilayer CeO2/Al/CeO2 resistive random-access memory. *Mater. Res. Express* **2020**, *7*, 16307−9.
(143) Lv, F.; Ling, K.; Zhong, T.; Liu, F.; Liang, X.; Zhu, C.; Liu, J.; Kong, W. Multilevel Resistive Switching Memory Based on a CH3NH3PbI Cl-3-x(x) Film with Potassium Chloride Additives. *Nanoscale Res. Lett.* **2020**, *15*, 126−8.
(144) Mahapatra, R.; Horsfall, A. B.; Wright, N. G. Forming-Free Reversible Bipolar Resistive Switching Behavior in Al-Doped HfO2Metal-Insulator-Metal Devices. *J. Electron. Mater.* **2012**, *41*, 656−659.
(145) Zhao, X.; Li, Y.; Ai, C.; Wen, D. Resistive Switching Characteristics of Li-Doped ZnO Thin Films Based on Magnetron Sputtering. *Materials* **2019**, *12*, 1282−11.
(146) Parreira, P.; Paterson, G. W.; McVitie, S.; MacLaren, D. A. Stability, bistability and instability of amorphous ZrO2 resistive memory devices. *J. Phys. D: Appl. Phys.* **2016**, *49*, 95111.
(147) Zhang, X.; Xu, L.; Zhang, H.; Liu, J.; Tan, D.; Chen, L.; Ma, Z.; Li, W. Effect of Joule Heating on Resistive Switching Characteristic in AlOx Cells Made by Thermal Oxidation Formation. *Nanoscale Res. Lett.* **2020**, *15*, 11−8.
(148) Lim, E.; Ismail, R. Conduction Mechanism of Valence Change Resistive Switching Memory: A Survey. *Electronics* **2015**, *4*, 586−613.
(149) Lin, K.; Hou, T.; Shieh, J.; Lin, J.; Chou, C.; Lee, Y. Electrode dependence of filament formation in HfO2 resistive-switching memory. *J. Appl. Phys.* **2011**, *109*, 084104.
(150) Harada, T.; Ohkubo, I.; Tsubouchi, K.; Kumigashira, H.; Ohnishi, T.; Lippmaa, M.; Matsumoto, Y.; Koinuma, H.; Oshima, M. Trap-controlled space-charge-limited current mechanism in resistance switching at Al/Pr(0.7)Ca(0.3)MnO(3) interface. *Appl. Phys. Lett.* **2008**, *92*, 222113−3.
(151) Child, C. D. Discharge From Hot CaO. *Phys. Rev. (Series I)* **1911**, *32*, 492−511.
(152) Langmuir, I. The Effect of Space Charge and Residual Gases on Thermionic Currents in High Vacuum. *Phys. Rev.* **1913**, *2*, 450−486.
(153) Rose, A. Space-Charge-Limited Currents in Solids. *Phys. Rev.* **1955**, *97*, 1538.
(154) Mott, N. F.; Gurney, R. W. *Electronic processes in ionic crystals*; Oxford Univ. Press, London, U.K., 1948.
(155) Zhu, Y. B.; Ang, L. K. Analytical re-derivation of space charge limited current in solids using capacitor model. *J. Appl. Phys.* **2011**, *110*, 94514−4.
(156) Mark, P.; Helfrich, W. SPACE-CHARGE-LIMITED CURRENTS IN ORGANIC CRYSTALS. *J. Appl. Phys.* **1962**, *33*, 205.
(157) Frenkel, J. On pre-breakdown phenomena in insulators and electronic semi-conductors. *Phys. Rev.* **1938**, *54*, 647−648.
(158) Gibson, G. A.; Musunuru, S.; Zhang, J.; Vandenberghe, K.; Lee, J.; Hsieh, C.-C.; Jackson, W.; Jeon, Y.; Henze, D.; Li, Z.; Stanley Williams, R. An accurate locally active memristor model for S-type negative differential resistance in NbOx. *Appl. Phys. Lett.* **2016**, *108*, 23505.
(159) Young, P. DC ELECTRICAL-CONDUCTION IN THIN TA2O5 FILMS.1. BULK-LIMITED CONDUCTION. *J. Appl. Phys.* **1976**, *47*, 235−241.
(160) Walczyk, C.; Wenger, C.; Sohal, R.; Lukosius, M.; Fox, A.; Dabrowski, J.; Wolansky, D.; Tillack, B.; Mussig, H.-J.; Schroeder, T. Pulse-induced low power resistive switching in HfO2 metal-insulator-metal diodes for nonvolatile memory applications. *J. Appl. Phys.* **2009**, *105*, 114103.
(161) Giovinazzo, C.; Sandrini, J.; Shahrabi, E.; Celik, O. T.; Leblebici, Y.; Ricciardi, C. Analog Control of Retainable Resistance Multistates in HfO2 Resistive-Switching Random Access Memories (ReRAMs). *Appl. Electron. Mater.* **2019**, *1*, 900−909.
(162) Funck, C.; Marchewka, A.; Baeumer, C.; Schmidt, P. C.; Mueller, P.; Dittmann, R.; Martin, M.; Waser, R.; Menzel, S. A Theoretical and Experimental View on the Temperature Dependence of the Electronic Conduction through a Schottky Barrier in a Resistively Switching $SrTiO_3$-based Memory Cell. *Adv. Electron. Mater.* **2018**, *4*, 1800062.
(163) Schroeder, H. Poole-Frenkel-effect as dominating current mechanism in thin oxide films—An illusion?! *J. Appl. Phys.* **2015**, *117*, 215103.
(164) Chen, X.; Hu, W.; Li, Y.; Wu, S.; Bao, D. Complementary resistive switching behaviors evolved from bipolar TiN/HfO2/Pt device. *Appl. Phys. Lett.* **2016**, *108*, 053504.
(165) Li, Y.; Pan, X.; Zhang, Y.; Chen, X. Write-Once-Read-Many-Times and Bipolar Resistive Switching Characteristics of TiN/HfO2/Pt Devices Dependent on the Electroforming Polarity. *IEEE Electron Device Lett.* **2015**, *36*, 1149−1152.
(166) Ismail, M.; Batool, Z.; Mahmood, K.; Rana, A. M.; Yang, B. D.; Kim, S. Resistive switching characteristics and mechanism of bilayer HfO2/ZrO2 structure deposited by radio-frequency sputtering for nonvolatile memory. *Results Phys.* **2020**, *18*, 103275−8.
(167) Chen, P. H.; Su, Y. T.; Chang, F. C. Stabilizing Resistive Switching Characteristics by Inserting Indium-Tin-Oxide Layer as Oxygen Ion Reservoir in HfO2-Based Resistive Random Access Memory. *IEEE Trans. Electron Devices* **2019**, *66*, 1276−1280.
(168) Sze, S. M.; Ng, K. K. *Physics of Semiconductor Devices*; Wiley, 2007.
(169) Padovani, F.; Stratton, R. Field and thermionic-field emission in Schottky barriers. *Solid-State Electron.* **1966**, *9*, 695−707.
(170) Fowler, R.; Nordheim, L. Electron emission in intense electric fields. *Proc. R. Soc. London* **1928**, *119*, 173−181.
(171) Wentzel, G. Eine Verallgemeinerung der Quantenbedingungen für die Zwecke der Wellenmechanik. *Eur. Phys. J. A* **1926**, *38*, 518−529.
(172) Kramers, H. A. Wellenmechanik und halbzahlige Quantisierung. *Eur. Phys. J. A* **1926**, *39*, 828.
(173) Lee, E.; Gwon, M.; Kim, D. W.; Kim, H. Resistance state-dependent barrier inhomogeneity and transport mechanisms in resistive-switching Pt/SrTiO3 junctions. *Appl. Phys. Lett.* **2011**, *98*, 132905−3.
(174) Funck, C.; Menzel, S. An atomistic view on the Schottky barrier lowering applied to SrTiO3/Pt contacts. *AIP Adv.* **2019**, *9*, 045116.
(175) Brandbyge, M.; Mozos, J.; Ordejon, P.; Taylor, J.; Stokbro, K. Density-functional method for nonequilibrium electron transport. *Phys. Rev. B: Condens. Matter Mater. Phys.* **2002**, *65*, 165401−17.
(176) Stradi, D.; Martinez, U.; Blom, A.; Brandbyge, M.; Stokbro, K. General atomistic approach for modeling metal-semiconductor interfaces using density functional theory and nonequilibrium Green's function. *Phys. Rev. B: Condens. Matter Mater. Phys.* **2016**, *93*, 155302.
(177) Funck, C.; Schmidt, P. C.; Baeumer, C.; Dittmann, R.; Martin, M.; Waser, R.; Menzel, S. Atomistic Investigation of the Schottky Contact Conductance Limits at SrTiO3 based Resistive Switching Devices. In *2018 Non-Volatile Memory Technology Symposium (NVMTS)*, 2018; pp 1−4.
(178) Marchewka, A.; Roesgen, B.; Skaja, K.; Du, H.; Jia, C. L.; Mayer, J.; Rana, V.; Waser, R.; Menzel, S. Nanoionic Resistive Switching Memories: On the Physical Nature of the Dynamic Reset Process. *Adv. Electron. Mater.* **2016**, *2*, 1500233−13.
(179) Marchewka, A.; Waser, R.; Menzel, S. A 2D Axisymmetric Dynamic Drift-Diffusion Model for Numerical Simulation of Resistive Switching Phenomena in Metal Oxides. In *2016 International Conference On Simulation of Semiconductor Processes and Devices (SISPAD)*, Nuremberg, Germany, September 6−8, 2016; pp 145−148.
(180) Simmons, J. G. Electric Tunnel Effect between Dissimilar Electrodes Separated by a Thin Insulating Film. *J. Appl. Phys.* **1963**, *34*, 2581.
(181) Fantini, A.; Wouters, D. J.; Degraeve, R.; Goux, L.; Pantisano, L.; Kar, G.; Chen, Y.-Y.; Govoreanu, B.; Kittl, J. A.; Altimime, L.;

https://doi.org/10.1021/acsaelm.1c00398
ACS Appl. Electron. Mater. 2021, 3, 3674−3692

Jurczak, M. Intrinsic switching behavior in HfO_2 RRAM by fast electrical measurements on novel 2R test structures. *Proc. 4th IEEE Int. Memory Workshop* **2012**, 1−4.
(182) Muenstermann, R.; Menke, T.; Dittmann, R.; Waser, R. Coexistence of Filamentary and Homogeneous Resistive Switching in Fe-doped $SrTiO_3$ Thin-Film Memristive Devices. *Adv. Mater.* **2010**, *22*, 4819−4822.
(183) Ielmini, D.; Waser, R. *Resistive Switching-From Fundamentals of Nanoionic Redox Processes to Memristive Device Applications*; Wiley-VCH, 2016.
(184) Schönhals, A.; Rosario, C. M. M.; Hoffmann-Eifert, S.; Waser, R.; Menzel, S.; Wouters, D. J. Role of the Electrode Material on the RESET Limitation in Oxide ReRAM Devices. *Adv. Electron. Mater.* **2018**, *4*, 1700243−11.
(185) Miao, F.; Yang, J. J.H.; Borghetti, J.; Medeiros-Ribeiro, G.; Williams, R. S. Observation of two resistance switching modes in TiO_2 memristive devices electroformed at low current. *Nanotechnology* **2011**, *22*, 254007−7.
(186) Shibuya, K.; Dittmann, R.; Mi, S.; Waser, R. Impact of defect distribution on resistive switching characteristics of Sr_2TiO_4 thin films. *Adv. Mater.* **2010**, *22*, 411−414.
(187) Menzel, S.; Waters, M.; Marchewka, A.; Böttger, U.; Dittmann, R.; Waser, R. Origin of the Ultra-nonlinear Switching Kinetics in Oxide-Based Resistive Switches. *Adv. Funct. Mater.* **2011**, *21*, 4487−4492.
(188) Mitra, C.; Lin, C.; Robertson, J.; Demkov, A. A. Electronic structure of oxygen vacancies in SrTiO3 and LaAlO3. *Phys. Rev. B: Condens. Matter Mater. Phys.* **2012**, *86*, 155105−8.
(189) Ricci, D.; Bano, G.; Pacchioni, G.; Illas, F. Electronic structure of a neutral oxygen vacancy in SrTiO3. *Phys. Rev. B: Condens. Matter Mater. Phys.* **2003**, *68*, 224105.
(190) Yang, J. J.; Strachan, J. P.; Miao, F.; Zhang, M.; Pickett, M. D.; Yi, W.; Ohlberg, D. A. A.; Medeiros-Ribeiro, G.; Williams, R. S. Metal/TiO2 interfaces for memristive switches. *Appl. Phys. A: Mater. Sci. Process.* **2011**, *102*, 785−789.
(191) Lin, Y. B.; Yan, Z. B.; Lu, X. B.; Lu, Z. X.; Zeng, M.; Chen, Y.; Gao, X. S.; Wan, J. G.; Dai, J. Y.; Liu, J. Temperature-dependent and polarization-tuned resistive switching in Au/BiFeO3/SrRuO3 junctions. *Appl. Phys. Lett.* **2014**, *104*, 143503−5.
(192) Procel, L. M.; Trojman, L.; Moreno, J.; Crupi, F.; Maccaronio, V.; Degraeve, R.; Goux, L.; Simoen, E. Experimental evidence of the quantum point contact theory in the conduction mechanism of bipolar HfO2-based resistive random access memories. *J. Appl. Phys.* **2013**, *114*, 74509.
(193) Graves, C. E.; Davila, N.; Merced-Grafals, E. J.; Lam, S.-T.; Strachan, J. P.; Williams, R. S. Temperature and field-dependent transport measurements in continuously tunable tantalum oxide memristors expose the dominant state variable. *Appl. Phys. Lett.* **2017**, *110*, 123501.
(194) Puglisi, F. M.; Zagni, N.; Larcher, L.; Pavan, P. Random Telegraph Noise in Resistive Random Access Memories: Compact Modeling and Advanced Circuit Design. *IEEE Trans. Electron Devices* **2018**, *65*, 2964−2972.
(195) Wiefels, S.; Bengel, C.; Kopperberg, N.; Zhang, K.; Waser, R.; Menzel, S. HRS Instability in Oxide based Bipolar Resistive Switching Cells. *IEEE Trans. Electron Devices* **2020**, *67*, 4208−4215.
(196) Raghavan, N.; Degraeve, R.; Goux, L.; Fantini, A.; Wouters, D. J.; Groeseneken, G.; Jurczak, M. RTN Insight to Filamentary Instability and Disturb Immunity in Ultra-Low Power Switching HfO_x and AlO_x. *Proceedings of the 2013 Symposium on VLSI Technology*, 2013; pp T164−T165.
(197) Troullier, N.; Martins, J. Efficient pseudopotentials for plane-wave calculations. *Phys. Rev. B: Condens. Matter Mater. Phys.* **1991**, *43*, 1993.
(198) Hamann, D. Generalized Norm-Conserving Pseudopotentials. *Phys. Rev. B: Condens. Matter Mater. Phys.* **1989**, *40*, 2980−2987.
(199) Raab, N.; Bäumer, C.; Dittmann, R. Impact of the cation-stoichiometry on the resistive switching and data retention of $SrTiO_3$ thin films. *AIP Adv.* **2015**, *5*, 047150.
(200) Jülich Supercomputing Centre.. JURECA: Modular supercomputer at Jülich Supercomputing Centre. *J. Large-Scale Res. Facilities* **2018**, *4*, A132.

https://doi.org/10.1021/acsaelm.1c00398
ACS Appl. Electron. Mater. 2021, 3, 3674−3692